

Accepted Manuscript

The “eye of Africa” (Richat dome, Mauritania): An isolated Cretaceous alkaline-hydrothermal complex

Guillaume Matton, Michel Jébrak

PII: S1464-343X(14)00097-1

DOI: <http://dx.doi.org/10.1016/j.jafrearsci.2014.04.006>

Reference: AES 2018

To appear in: *African Earth Sciences*

Received Date: 12 April 2013

Revised Date: 7 April 2014

Accepted Date: 8 April 2014



Please cite this article as: Matton, G., Jébrak, M., The “eye of Africa” (Richat dome, Mauritania): An isolated Cretaceous alkaline-hydrothermal complex, *African Earth Sciences* (2014), doi: <http://dx.doi.org/10.1016/j.jafrearsci.2014.04.006>

This is a PDF file of an unedited manuscript that has been accepted for publication. As a service to our customers we are providing this early version of the manuscript. The manuscript will undergo copyediting, typesetting, and review of the resulting proof before it is published in its final form. Please note that during the production process errors may be discovered which could affect the content, and all legal disclaimers that apply to the journal pertain.

**The “eye of Africa” (Richat dome, Mauritania):
An isolated Cretaceous alkaline-hydrothermal complex**

Guillaume Matton

Michel Jébrak*
Jebrak.michel@uqam.ca

*Department of Earth and Atmospheric Sciences, Université du Québec à Montreal,
201 President-Kennedy, Montreal, Quebec H3C 3P8, Canada.
Telephone; 1 514 987 3000, 3986#
Fax : 1 514 987 7749*

** Corresponding author*

Submitted to Journal of African Earth Sciences

33 **Keywords:** *alkaline complex, hydrothermalism, Cretaceous, petrology, structural*

34 *geology*

35

ACCEPTED MANUSCRIPT

36 Abstract

37 The Richat dome is a spectacular circular structure located in the Mauritanian part of
38 the Sahara Desert. The current erosion level of this igneous complex presents a wide
39 variety of contrasting extrusive and intrusive rocks from shallow to deep source regions
40 providing insight into the magmatic process at the origin of the complex.

41 The Richat is the superposition of a bimodal tholeiitic suite crosscut by carbonatitic
42 and kimberlitic magmatic rocks. The bimodal series is characterized by two concentric
43 gabbroic ring dikes and two extrusive rhyolitic centers representing the remnant of two
44 maar systems. Silica undersaturated magmas occur as carbonatite dikes, a kimberlite
45 plug, and kimberlite sills extruded along the old regional anisotropies filling NNE-SSW
46 dextral strike-slip faults and en-echelon tension gashes. An intense low-temperature
47 hydrothermal event affected the Richat area. It is responsible, notably, for the karst-
48 collapse central mega-breccia, the alteration of the rhyolites, the potassic alteration of the
49 gabbros and the stable isotope enrichment in the carbonatites. A piston-like collapse is
50 proposed to explain the contrast existing between the central and outer part of the Richat.

51 Structural inheritance played an important role in the history of the Richat complex.
52 Pre-existing anisotropies acted as a pathway for the ascent of asthenospheric and sub-
53 continental melts and allowed the coexistence of alkaline and tholeiitic magmas within
54 the same igneous complex.

55

56

57 **1. Introduction**

58 Mauritania hosts the *Guelb er Richat*, a fascinating circular structure also called the
59 “eye of Africa”. The Richat complex appears as a large eroded dome, at least 40 km in
60 diameter including rare exposures of volcanic and intrusive rocks from contrasting
61 erosion levels. It consists of gabbroic ring dikes, kimberlitic intrusions, carbonatites dikes
62 and felsic volcanic rocks and encloses a kilometer-scale siliceous breccia in its center
63 crosscutting Proterozoic and Paleozoic platform sediments.

64 This complex has been studied by several workers but its understanding remains very
65 poor. Early workers cited the crater-like shape and the high-relief centre, with its
66 kilometer-scale breccias, as evidence of a meteorite impact (e.g., Cailleux et al., 1964) or
67 explained the structure as the result of basement adjustments and plutonic doming
68 (Destombes and Plote, 1962; Dietz et al., 1969; Boussaroque, 1975). The debate has also
69 focussed on the origin of the igneous rocks. “Analcimolite”, a rock containing up to more
70 than 75% analcime has been variously interpreted as an extrusive volcanic rock with
71 primary analcime (Bardossy et al., 1963), a hot spring deposit (Fabre, 1999), a weathered
72 sediment (Boussaroque, 1975) and a secondary deposit generated by the replacement of
73 rhyolite, rhyolitic tuff, or sediment (Fudali, 1973). Gabbroic rocks were also poorly
74 understood and thought to be associated to the Triassic/Jurassic extensive tholeiitic
75 magmatism of West Africa (Trompette, 1973a; Netto et al., 1992) whereas the core
76 megabreccia remained unexplained.

A first study on breccias was presented by Matton et al. (2005) and Matton (2008) and demonstrated their Cretaceous hydrothermal origin. The overall geodynamic context was presented in Matton and Jébrak (2009), showing the abundance of alkaline systems around 100 Ma and suggesting the role of reactivated pre-existing lithospheric structures during the opening of the Atlantic Ocean. Here, we present new petrological, structural, geophysical and geochemical data collected from three missions on the Richat structure. New features are documented, notably the felsic volcanic basins and associated maar systems, and the interpretation of the caldera in the centre of the dome. This paper proposes an overall understanding of the wide variety of rocks and their possible relations into a comprehensive model of the magmatic system. We demonstrate that the Richat magmatism involved a bimodal tholeiitic series crosscut by silica undersaturated carbonatitic and kimberlitic magmas. Our data show the importance of the regional structural system on the development of the caldera.

2. Geological and structural setting

The Taoudenni Basin, of Proterozoic to Carboniferous age, is one of the major structural units of the West African craton and covers about two million square kilometers (Bronner, 1992; Abdelsalam et al., 2011). The basin is bounded by the Reguibat and Man ridges of Archean age to the north and to the south respectively (Fig. 1A) and is bordered on its western side by the Pan-African Mauritanides orogen (Michard et al., 2010). Sedimentary units are composed of continental shelf marine sediments with terrestrial intercalations. The stratigraphy of the basin begins with a Late Proterozoic (~1100–1000 Ma) sequence consisting of sandstone, mudstone, dolomite, and dolomitic limestone (Trompette, 1973b; Rooney et al., 2010). Overlying an angular unconformity,

the Proterozoic (~650 Ma) to Cambrian-Ordovician sequence is composed of alternating layers of limestone, dolomitic limestone, sandstone, chert, and mudstone. The summital units range in age from Late Ordovician to Carboniferous, and are mostly composed of sandstone with intercalations of mudstone and limestone. Stromatolites have been observed in late Precambrian and Cambrian-Ordovician units.

The Richat complex forms a large eroded dome more than 40 km in diameter in the northern part of the Taoudenni Basin. Sedimentary rocks range in age from Late Proterozoic towards the center of the dome to Ordovician (Chinguetti Sandstone) on its periphery. The layers dip outward at 10°-20°. Erosion has created three concentric high-relief (~20-30m) ridges in harder quartzitic units (Fig. 1B). In this paper the use of “inner part” refers to the area located inside the innermost ridge. A central topographical depression occurs in the core of the structure where the only crest comes from the breccias unit. The Richat structure has a slightly elliptical shape. Measures of the ellipticity (length of minor axis / length of major axis) give values ranging from 0.87-0.88 for both the inner part and the entire structure with the major axis oriented NE-SW.

Two major sets of regional fracture networks are recognized on satellite imagery and on ground (Fig. 1B). The first one is oriented approximately NNE-SSW and could be related to the Pan-African event (600 Ma; Netto et al., 1992; Poupeau et al., 1996). The other set of fractures strikes ~ ENE-WSW (N70°–N90°) and crosscuts Pan-African structures (Bayer and Lesquer, 1978). Moreover, a deep narrow NE-SW trough is recognized between the Richat dome and the Mauritanides orogen (Bronner, 1992). The trough corresponds to the greatest thickness (~3500 m) of the Late Proterozoic sequence (1100-650 Ma) in the Taoudenni Basin and is interpreted as an aulacogen structure

related to the Pan-African I rift event in the Mauritanides (~750-660 Ma; Villeneuve and Cornée, 1994; Villeneuve, 2008).

Within the dome, the fractures can be classified into three sets; two are planar and trending subparallel to regional fractures, and one appears concentric and limited to the inner part of the Richat (Fig. 1B). NNE-SSW faults display dextral movements as well as minor vertical offsets. The dextral component of these faults is demonstrated by the displacement of the external ring dike, the en-echelon pattern observed in some carbonatite dikes and by the dextral movement in wall rock striations of N15–20° carbonatite dikes. The ENE-WSW faults display sinistral movement, clearly shown by the offset of the external ridges in satellite image (Fig. 1B). Since satellite images demonstrate the extension of local fractures in the surrounding country rocks outside the dome, we interpret them to be related to the large-scale subparallel regional fracture networks.

Usually covered by sand and/or alluvium, the central concentric fractures are not directly observed in the field, but subvertical normal displacements are inferred from stratigraphic misfits, repetitions of central sedimentary sequences and duplication of the breccia unit. The breccia is found in the core and in the periphery of the inner central depression. Cut by previously-described NNE-SSW and ENE-WSW fracture sets, circular faults appear discontinuous and do not form a perfect concentric pattern. Post-doming movements are clearly visible in the Richat structure with the crosscutting and displacement of doming-related ridges, ring dikes and late-stage felsic volcanic rocks (described below) by the two fracture sets for which reactivation processes are described until the Holocene (Poupeau et al., 1996). Therefore, the Richat dome appears to be

characterized by the overprinting of an “old” regional fracture networks, doming-related structures and post-doming movements.

3. Petrology

Different igneous rock series have been reported previously from the Richat dome, which includes quartz-gabbros and dolerites, diorites, aplites and granites (Blanc and Pomerol, 1973). These authors also mentioned abnormal values of up to 8% K₂O for the gabbroic rocks. However, our field work did not allow the recognition of the more evolved part of this series (aprites and granites). Large-scale hydrothermal potassic enrichment has been documented in the Richat dome (see section 3.2) and this may have caused previous workers to call certain altered rocks “aprites and granites”. Four types of igneous rocks are recognized and mapped: rhyolitic volcanic rocks, gabbros, carbonatites and kimberlites. Gabbros and kimberlites are clearly shown on the regional magnetic survey (Fig. 1C).

3.1 Rhyolite

Rhyolitic volcanic rocks occupy the inner part of the Richat dome. It is noteworthy that volcanic rocks are all restricted to the central part of the dome. They consist of lava flows and volcanoclastic rocks spatially associated with two eruptive centers located to the SW and to the NE of the core, respectively (Fig. 1D). The first one is a ~2.5 km diameter volcanic crater that crosscuts the inner gabbroic basaltic ring dike, forming a circular depression filled by sebkha deposits. The crater ring is clearly visible from satellite images and is characterized by up to 2 m-thick layer of coarse ejecta at its base, overlain by tuffs and lava flows. The coarse ejecta layer consists of fragmented volcanic

material in a completely hematized matrix (Fig. 2A). The second eruptive center forms a small partially preserved volcanic basin (Fig. 2B) that contains brecciated to conglomeratic rocks, lavas and tuffs (Fig. 2C) lying with angular unconformity on the sedimentary units. Eruptive rocks dip toward the center of the Richat dome at low angles ($\sim 15^{\circ}$ - 27°). Both low relief craters are interpreted as the remnant of two maar systems.

All volcanic rocks lie on an erosional unconformity and appear to postdate all other igneous phases. The stratigraphy of volcanic units is consistent from the southwestern crater area to the northeastern crater but the ejecta ring is only found at the southwestern one. A typical cross-section of the volcanic rocks includes four main gradational units. Some units may be absent locally due to lateral variations (Fig. 3).

The poorly sorted, matrix-supported basal unit is ~ 1 - 4 m thick and ranges in texture from a breccia to a conglomerate. It contains fragments of sedimentary rocks in a tuffaceous matrix. The abundance of country rock clasts and their heterogeneous composition suggest that they were derived from the underlying sedimentary rocks by subsurface explosions. Fragments reach 30 cm in diameter and include sandstone, quartzite, chert and red jasper. Jasper always appears in the form of small rounded fragments, less than 1 cm in diameter, and such clasts have not been found elsewhere in outcrops at Richat; they may represent an underlying sedimentary unit. The roundness of the fragments and the thickness of the unit increase with distance to craters creating a transition from breccia (angular fragments) near the crater to a conglomeratic facies away from it.

Unit 2 is a 3-4 m-thick quartz-phyric rhyolite in sharp contact with unit 1 (Fig. 2C) and may represent a distinct lava flow. The texture is uniform with 5-10% euhedral

quartz phenocrysts (< 1 mm to 2 mm) in an analcime-rich groundmass. Some quartz crystals appear partially corroded by analcime and calcite. Small (sub-millimeter) vesicles occupy 1-5% of the rock.

Unit 3 is ~5-6 m-thick and composed of up to 70% analcime glomerocrysts and of up to 40% vesicles, up to 5 cm in diameter. Glomerocrysts are frequently characterized by a core of analcime and a rim of nordstrandite + analcime (Fig. 4A) but may also be entirely composed of analcime. An increase is observed in the size and proportion of vesicles from base to top, whereas the glomerocrysts decrease in size but not in proportion. Near the contact with the underlying rhyolite, the rock contains ~70% glomerocrysts (1-3 mm) and ~15-20% vesicles (~0.5 mm) respectively. Progressing upward, vesicles reach 1 to 1.5 cm. The upper part of the section contains so many vesicles (~40%) that the rock has a pumiceous aspect (Fig. 2E). Quartz phenocrysts are present but are less abundant and smaller in size than in the rhyolite. Small vesicles from the bottom part of the unit are generally filled by analcime whereas progressing to the upper part, large vesicles show variable degree of filling with botroidal analcime and nordstrandite sometimes giving an “egg shell” texture due to differential weathering (Fig. 2D).

Unit 4 is generally 3 m-thick and is characterized by the presence of large vertically-elongated lithophysae. Lithophysae are up to 1 m high and 5 cm wide (Fig. 2G). They are always oxidized and appear purple or more rarely yellowish to brown. In contrast to unit 3, porosity does not exceed 10% of the rock and vesicles are much smaller, generally <1 mm. When they are present, vesicles form vertical cavity streaks. Glomerocrysts are present but also less abundant (< 20%) and smaller (<1 mm) than in the underlying unit. In horizontal outcrops, diffusion structures give spectacular purple concentric rings that

may reach 25 cm in diameter (Fig. 2F). Pervasive oxidation also occurs as large purple stains to completely oxidized outcrops. The latter may have developed in more porous rocks than the lithophysae facies. Quartz crystals are rare and always microcrystalline.

Hand specimens show a wide range of colors from cream or light beige through yellow to ochre and purple due to the variable presence of iron oxide. Variable proportion of quartz, analcime and nordstrandite accounts for 90 % of all volcanic rocks, with minor amount of dawsonite, calcite, K-feldspar, anatase and hematite. Some volcanic rocks contain so much analcime (more than 75%) that they were called “analcimolites” by Bardossy et al. (1963). In thin section, analcime occurs under two habitus; (1) fine-grained interstitial filling and veinlets (Fig. 4C) and (2) coarse-grained cavity fills (Fig. 4D) and glomerocrysts. Nordstrandite is microcrystalline and difficult to identify, been interlaced with analcime (Fig. 4A). Close association between analcime and gibbsite or analcime and dawsonite in the Richat has been previously suggested (Fudali, 1973; Boussaroque, 1975). Although the presence of dawsonite and gibbsite has been confirmed locally, X-ray diffraction (XRD) and scanning electron microscope (SEM) analyses show that the main mineral associated with analcime is in fact the $\text{Al}(\text{OH})_3$ polymorph of nordstrandite.

Early phases of alteration in the rhyolitic rocks are characterized by the replacement of quartz crystals by calcite and analcime (Fig. 4B, 4F). Neo-formed calcite was then replaced by analcime, accompanied or not by nordstrandite (Fig. 4E). In thin section, analcime and nordstrandite always appears as the last secondary mineral phases. It is plausible that when silica was unavailable in the system, excess aluminium formed nordstrandite. Table 1 shows this sequence of alteration. In weakly altered rhyolites, only

automorphous quartz and analcime-rich matrix is found with small amounts of K-feldspar, anatase and hematite. In the strongly altered rhyolites, quartz becomes scarcer and is replaced by calcite and analcime while dawsonite makes its first appearance, whereas in the highly altered sections, only analcime and nordstrandite remain with trace amounts of kaolinite, gibbsite, calcite, anatase and hematite.

3.2 Gabbro

Field mapping and aeromagnetic data have shown that gabbroic rocks form two concentric ring dikes (Fig. 1D). The internal ring dike is ~20 m in width and the external one ~50 m. They are located respectively ~3 km and ~7-8 km from the center of the structure. Gabbroic rocks are fine- (< 1 mm) to coarse-grained (\leq 1 cm) and show ophitic textures (Fig. 4H). Plagioclase consists of variable proportions of andesine, anorthite and albite, whereas pyroxenes are augite and diopside. Pyroxenes are partially replaced by amphiboles (actinote, hastingsite, pargasite), magnetite, biotite and chlorite, where chlorite is the last alteration phase, destroying biotite crystals. Minor proportions of quartz and muscovite are also found.

High-potassic intrusive rocks are found in the northern part of the structure. These rocks are characterized by a K_2O concentration of up to 6.13 wt % and a SiO_2 content ranging from 58.1 wt % to 60.4 wt %. Their occurrence is restricted to an area of about 100 m² corresponding to the northern part of a major NNE-SSW deformation zone responsible for the dextral shearing of the external gabbroic ring dike (Fig. 1B). These rocks have not been found elsewhere in the Richat dome. They are mainly composed of albite, microcline, quartz and chlorite with minor proportions of augite, biotite and magnetite. In thin section, secondary neoformed K-feldspar appears to corrode

plagioclase crystals (Fig. 4I). All the feldspars are strongly sericitized and pyroxenes are partly to totally replaced by chlorite and magnetite. Nevertheless, an ophitic texture is still recognizable. We interpret these rocks as hydrothermally altered gabbros. The exposure is poor in this sandy area, but potassic and silica enrichment seems to be related to fracturation zones inside the external gabbroic ring dike. These rocks may correspond to the aplites and granites mentioned by Blanc and Pomerol (1973) and may coincide with their reported high-K gabbros.

3.3 Carbonatite

Thirty-two carbonatite intrusions (dikes and less common sills) are recognized in the Richat structure. First identified by Woolley et al. (1984), carbonatite dikes were thought to be radial and synchronous with the doming or emplaced along the radial system of joints and faults generated by it. Even radial distributions of carbonatite dikes are a common feature in alkaline complexes such as in Alnö (Kresten, 1982), Powderhorn (Olson and Hedlund, 1981), and Gross Brückaros (Stachel et al., 1994), this assumption is implausible at the Richat since carbonatite dikes are all oriented N15-20° (Fig. 1B) and were emplaced in pre-existing NNE-SSW fracture sets. Further, their occurrence is limited to the southern part of the dome. None of the carbonatite dikes extent beyond the internal depression toward the central part of the Richat.

Dikes are generally ~300 m long and 1–4 m-wide. The carbonatites are massive and are mostly devoid of vesicles. Fresh rocks appear pale grey and weathered to a rusty-red to light brown color. Carbonate grain size is variable, ranging from fine to coarse subhedral to euhedral crystal grains sometimes included in less well-defined aphanitic carbonate groundmass. Dikes are mainly composed of dolomite and, in a minor

proportion, ankerite. Other components include quartz, apatite, barite, hematite, calcite and traces of pyrite. Values of up to 0.23 % Nb₂O₅ in whole-rocks geochemical analyses strongly suggest the presence of pyrochlore or others Nb-bearing minerals. Although the mineralogy of these dykes could represent a hydrothermal infilling, the abundance of Phosphorus and Niobium is more indicating of a primary magmatic assemblage.

Multiple magma injections in dikes are frequent and formed vertical banding. Vertical bands are of different colors according to the quantity of iron oxides and some have breccia envelopes. Breccia envelopes are generally 10-50 cm-wide and include angular to rounded country rock fragments (sandstone, chert, limestone and shale) as well as gabbroic clasts. Fragments are millimetre to decametric in size and some display corroded borders. Intensely corroded fragments are preferentially composed of quartzitic sandstone and chert. Note that enclaves of sediments are abundant in most of the dikes and not limited to the breccia envelopes. Carbonatite dikes are silicified and partially ankeritized. Contacts with country rocks are generally sharp without significant alteration or fenitization although pervasive silicification may be found locally. Tensional veinlets oriented N254° have also been found within the wall rocks of some dikes. Fission-track dating of apatite in the carbonatite yielded a Mid-Cretaceous emplacement age (99 ± 5 Ma; Poupeau et al., 1996).

3.4 Kimberlite

Kimberlitic rocks in the form of a plug and several sills and dikes were recognized in the northern part of the circular structure (Fig. 1B and 1C). The plug does not outcrop but a sample of a sill was recovered in a trench. The sill is highly altered and mainly composed of coarse (~10 mm) phlogopite. Other minerals are deeply weathered although

pyroxene and olivine remnants are found. X-ray diffraction (XRD) analyses reveal in order of importance: phlogopite, serpentine, smectite, chlorite, magnetite, hematite and amphibole. Unpublished dating of the kimberlite plug gave an age of about 99 Ma (T. Abdivall, personal commun.) that should be validated.

3.5 Central breccia

The center of the structure is occupied by a karst-collapse siliceous megabreccia body at least ~3 km in diameter and up to 40 m thick (Fig. 2H) host by Paleozoic limestone (Matton et al., 2005). The breccia forms a lens that thins at its extremities to only a few meters. This thinning is irregular and creates finger-like shapes. Breccia fragments are polymictic and include white to dark gray cherty material, quartz-rich sandstone, diagenetic cherty nodules, and stromatolitic limestone. Hydrothermal internal layered-sediments fill the breccias and are composed of quartz and automorphous neoformed K-feldspar. They are strongly enriched in alkaline elements (Sr, K, Rb and Ba, notably) in comparison to the detritic infilling of the upper part of the breccia revealing the large-scale hydrothermal system at the core of the Richat (Matton et al., 2005). K-feldspar from the hydrothermal sediment was dated using the $^{40}\text{Ar}/^{39}\text{Ar}$ method and yielded an integrated age of 98.2 ± 2.6 Ma (Matton et al, 2005).

The breccia body is intensely silicified. The silicification event was contemporaneous with the main breccia event but also continued afterward, as evidenced by the fact that both fragments and the internal sediments are extensively silicified, and that microcrystalline quartz cement fills the breccia cavities and intergranular spaces. The breccia was formed during karst dissolution and collapse where doming and the production of hydrothermal fluids were instrumental in creating a favorable setting for

dissolution. Further details can be found in Matton et al. (2005) and Matton (2008). Recent geochemical analysis have demonstrated large variations in trace elements composition with evidence of a high barium content, up to 700 ppm (Jesus et al., 2011), indicating low-temperature hydrothermal fluid circulation. The scale of this mega-breccia implies that huge amounts of hydrothermal fluids were produced at the very centre of the Richat dome.

4. Whole-rock major and trace elements compositions

Representative samples of the host rocks were selected in the field. Whole rock analyses of samples were performed by ACME Labs in Vancouver. Rare earth and refractory elements were determined by ICP mass spectrometry following a lithium metaborate/tetraborate fusion and nitric acid digestion of a 0.1 g sample. Results are given in Table 2.

4.1 Rhyolites

Volcanic rocks from the center of the Richat show extreme compositional variations, with SiO_2 values ranging from ~ 42.5 to 73.7 wt % (Fig. 5A). Moreover, K_2O contents appear abnormally low for rhyolites, with all values falling under 0.17 wt % whereas Na_2O concentrations are always high, ranging from 5.7 to 9.2 wt %. However, as described above, volcanic rocks show a suite of secondary minerals that record hydrothermal metasomatism (Table 1).

Figure 6 shows the variation of CaO , Na_2O and Al_2O_3 against SiO_2 . A decrease in silica appears correlated with an increase in CaO up to a critical point beyond which the CaO decreases abruptly. The CaO increase may represent the addition of calcite at the

expense of silica in the system whereas the CaO decrease occurs when calcite begins to be replaced by analcime. Sodium also increases with the diminution of silica content but decreases in the most silica-depleted rocks. This is reflected by the observed replacement of quartz and calcite by analcime, whereas in the advanced stages of alteration, sodium was not sufficient and excess alumina crystallized in nordstrandite

Insoluble alumina thus concentrates as a residual phase throughout the alteration process, since more material is removed than added (Fig. 6). In highly altered zones, increasing water circulation and alkali depletion may cause nordstrandite to dissolve and destabilize, favouring gibbsite as the most likely $\text{Al}(\text{OH})_3$ polymorph to be found (Dani et al., 2001). High gibbsite contents reported by Fudali (1973) may thus correspond to late-stage extremely altered rocks representing the end part of this alteration suite, or misidentified nordstrandite.

Alteration of rhyolitic lavas and tuffs by hydrothermal solutions thus appears the more likely process to produce the extrusive rocks outcropping at Richat, which contain up to 75% analcime. The recognition of an intense low-temperature hydrothermal event, thought to have strongly affected the Richat central area, also favours this origin for the “analcimolites”. Gupta and Fyfe (1975) demonstrated that alteration of rhyolite into analcime can be achieved with the involvement of saline fluids at temperatures of $\sim 150^\circ\text{C}$. The discovery of the two volcanic craters associated with the “analcimolites” also confirms the volcanic origin of these rocks and precludes the involvement of weathered sediments as reported by Boussaroque (1975). Our works therefore support the interpretation of Fudali (1973) suggesting that the “analcimolites” at Richat are the result of the alteration of rhyolites and rhyolitic tuffs.

4.2 Gabbros

The mafic ring dikes are relatively primitive melts, spanning a short compositional range of Mg# 56-62. They have low TiO_2 (0.7-1.3 wt %) and moderate MgO (6.3-7.6 wt %) content, and fairly high SiO_2 (46.5-52.2 wt %). No difference in geochemistry is discerned between external and inner ring dikes; this suggests that both ring dikes were generated from the same magma chamber and that the time interval between both dikes was small and did not allow differentiation to occur.

Figure 7 show the trace element concentrations in mafic dikes from the Richat, normalized to mid-ocean ridge basalts (MORB) and ocean island tholeiites (OIT), respectively. Analysed samples differ significantly from MORB compositions, but clearly show the similarity between these mafic rocks and oceanic-island tholeiites. Nevertheless, the Richat gabbros are enriched in Rb, Ba, Th and Pb and depleted in Ta, Nb, and Ti relative to the ocean-island tholeiites. Ta-Nb negative anomaly is as typical feature of subduction-related magmas but may also be the consequence of crustal contamination in continental flood basalt with the relative abundance of Rb and Th indicative of depth of contamination (Cox and Hawkesworth, 1985; Wilson, 1989; Taylor and McLennan, 1995). Comparing multi-element patterns of the Richat gabbros with the average amphibolite (upper crust) and granulite (lower crust) (Fig. 7C) suggests that gabbros from the Richat have been contaminated by upper crustal rocks. This is evidenced by the distinctive Th enrichment and confirmed on a Th/Yb versus Ta/Yb diagram (Fig. 8), where the Richat gabbros plot near the enriched mantle source, suggesting the involvement of subcontinental lithosphere or OIB source mantle in their

petrogenesis (Wilson, 1989) with high Th/Yb ratios which might be indicative of crustal contamination.

When compared with CAMP tholeiitic dikes from West Africa (Taoudenni Basin and Guinea; Fig. 7D), Richat gabbros are similar. Despite their relatively higher positive anomalies in Pb and Ba, which can be attributed to higher level of crustal contamination, Richat dikes are remarkably analogous with those from Low-Ti CAMP basalts, supporting their derivation from a similar mantle source. It is now widely accepted that Early Jurassic CAMP tholeiitic geochemical features are indicative of a heterogeneous source residing in metasomatized portions of the sub-continental lithospheric mantle (Pegram, 1990; Heatherington and Mueller, 1999; De Min et al., 2003; Jourdan et al., 2003; Verati et al., 2005). The younger Cretaceous Richat mafic igneous rocks may come from a similar source with a different extent of crustal contamination.

A bimodal suite at Richat is suggested by the presence of gabbroic ring dikes and rhyolites with no intermediate rocks observed (Fig. 9). This bimodal suite has a tholeiitic composition (Fig. 5B). The diagrams in figure 9 show the variation of major and trace element abundances as a function of the SiO₂ content in the bimodal series from the Richat. Mafic to felsic rocks display variation trends of decreasing MgO, FeO, CaO, TiO₂ and increasing Na₂O with higher SiO₂ content. As mentioned earlier, K₂O content in rhyolites appears abnormally low for a typical rhyolite and therefore, usual trend of increasing K₂O from mafic to evolved silicic magmas is not observed. This may be due to early destabilisation of K-bearing minerals. Abundance of the compatible trace elements (V, Ni, Sc, Sr) decline systematically from basalt to rhyolite (Fig. 9). In contrast, (High Field Strength) incompatible trace elements Nb and Y show little to no variation with

differentiation, whereas Zr abundance is highly variable in rhyolite. Moreover, Rubidium content of rhyolites is generally low (under 20 ppm) and correlation between Rubidium and Silica is absent which may be another indication of early destabilisation of K-bearing minerals and mobilisation of Rb by late fluid circulation.

Chondrite-normalized rare earth elements (REE) data for rhyolites and gabbros are plotted on figure 10A. Both rock types show flat pattern of heavy rare earth elements (HREE) with enrichment in light rare earth elements (LREE) suggesting a same or similar parental magma. Rhyolites display similar HREE concentrations relative to the gabbros but higher LREE contents. Little to no Eu anomaly is present, indicating that fractionation of feldspar in the source is limited. The relative HREE concentrations in the gabbros also suggest that garnet is absent from the source (Wilson, 1989). LREE enrichment may either be a consequence of crustal contamination or their derivation from enriched mantle sources.

4.3 Undersaturated rocks

Carbonatites from the Richat dome show beforosite (magnesio-carbonatite) affinities (Fig. 10C). They are strongly enriched in LREE and plot within the field of carbonatites (Fig. 10B) with La/Yb ratios ranging between 80 and 222. This confirms the previous observation made by Woolley et al. (1984) on the carbonatitic nature of three dikes from the Richat. Ba and Nb yield high values, up to 9558 ppm and 1600 ppm respectively. The high Ba content is related to the presence of observed barite, whereas the high Nb values suggest the presence of pyrochlore or others Nb-bearing minerals. The kimberlitic sill falls within the world kimberlitic rock domain and displays as well a relatively steep REE profile with a La/Yb ratio of 47.

5. Carbon and oxygen isotopic compositions

Carbon and oxygen isotope ratios were measured on a MicroMass Isoprime mass spectrometer at the Stable Isotopes Laboratory at GEOTOP–UQAM in Montréal, Canada. Circa 1mg of each powdered sample was weighted in glass vials and reacted individually with H_3PO_4 after heating to 90°C for 1h. The released CO_2 was collected through a coldfinger and analyzed using an in-house reference gas. Samples were calibrated to VPDB (Vienna Pee Dee Belemnite) using standards NBS-18 and UQ6. Errors are about 0.05‰ for both $\delta^{13}\text{C}$ and $\delta^{18}\text{O}$.

The carbon and oxygen isotope compositions of carbonatite dikes from the Richat are plotted in figure 11. None of the samples lie within the field of the Primary Igneous Carbonatites (PIC; Reid and Cooper, 1992). The $\delta^{13}\text{C}$ values are close to slightly higher than the PIC range, but the $\delta^{18}\text{O}$ values are clustered at much higher values. It is thus clear that these carbonatites have not retained their primary isotopic signature. Deines (1989) and Reid and Cooper (1992) documented a positive correlation between $\delta^{13}\text{C}$ and $\delta^{18}\text{O}$ in the 5 to 15‰ range for the carbonatites. Deines (1989) has attributed this correlation to the effect of Rayleigh fractionation but specify, however, that Rayleigh fractionation is unlikely to have produced $\delta^{18}\text{O}$ values greater than $+17\text{‰}$. The more extreme $\delta^{18}\text{O}$ values are then attributed to secondary processes involving fluid-rock interaction in a low-temperature hydrothermal system (Deines, 1989; Keller and Hoefs, 1995; Castorina et al., 1997; Onuonga et al, 1997; Bouabdellah et al., 2010). Correlations between $\delta^{18}\text{O}$ and $\delta^{13}\text{C}$ values suggest a CO_2 -rich fluid composition for this event. Hydrothermal processes are also supported by the strong presence of barite (up to 10000 ppm Ba) in the carbonatites dikes from the Richat, a typical product of late-stage

crystallisation of carbonatites deposited by circulating hydrothermal fluids (Woolley et al., 1984; Mariano, 1989).

6. Chronology

Field observations and available radiometric dating allow the following chronology of magmatic events to be proposed, from the oldest to the youngest:

1- Intrusive gabbros

2- Intrusive carbonatites (85 ± 5 , Netto et al., 1992; 99 ± 5 Ma; Poupeau et al., 1996), breccia and hydrothermal sediments infilling (98.2 ± 2.6 Ma; Matton et al, 2005)

3- Extrusive rhyolites

No radiometric ages currently exist for the gabbros and rhyolites. However, gabbros clearly appear as the first magmatic phase in the Richat dome and are perfectly centered on the dome structure. These ring dikes are crosscut and displaced by the main NNE-SSW and ENE-WSW fracture sets. Moreover, they are crosscut by NNE-SSW carbonatite dikes and thus older than 99 ± 5 Ma. Consequently, a reactivation of the NNE-SSW deep pre-existing lineament (Pan-African) could have occurred around 99 Ma, allowing the carbonatite magmas to raise and fill the fractures. The kimberlite plug has been dated by Asthon Mining Inc. to ~99 Ma in 2005. However, information on the age dating method and the analytical error is not available. Moreover, its position in the northern part of the structure does not allow relative chronology with the other magmatic phases. The rhyolitic rocks appear to postdate all other igneous phases. Located in the central part of the structure, they do not show any evidence of silicification and are likely to postdate the large-scale siliceous hydrothermal event that forms the core megabreccia.

Taking into account that large bimodal volcanoes are generally active ≤ 10 Ma such as in the Mont-Dore, Cantal, and Siroua, massifs (Berrahma and Delaloye, 1989; Wilson and Downes, 2006) and that mafic and felsic magmas appear to be respectively the first and the final magmatic events at Richat, we may assume that approximate ages of the system, from mafic to felsic events, would be between 104 and 94 Ma.

7. Discussion

7.1 Piston caldera

The center of the Richat structure is characterized by circular fractures creating stratigraphic misfits as well as repetitions of sedimentary sequences and duplication of the breccia unit (Matton, 2008). In addition, it is noteworthy that all intrusive rocks are in the external part of the complex whereas volcanic rocks are almost exclusively restricted to the central part. This strongly suggests a model of piston-like caldera collapse preserving the central part from erosion.

Measures of the ellipticity (length of minor axis / length of major axis) give values ranging from 0.87-0.88 for both the inner depression and the entire structure with the major axis oriented NE-SW. As suggested by Acocella (2007), if we accept that the configuration of a caldera in map view reflects the shape of the underlying magma chamber, the elongation at the Richat caldera may be due to two factors:

- 1- Stretching of an original subcircular caldera (or reservoir) under regional extension (Bosworth et al., 2000);
- 2- The presence of a pre-existing NE-SW structure.

If the non-circular shape of the structure is the result of symmetrical magmatic doming overprinted by a regional stress field, the emplacement of the magma chamber and the caldera should have occurred in a transtensional environment with the main stress oriented ~NW-SE. However, the structural faulting imply a regional-scale NE-SW-oriented horizontal main stress in a conjugated pattern (Matton et al., 2005) and therefore, the first hypothesis appears unlikely. Moreover, the Richat structure is located over a pre-existent NE-SW aulacogenous structure (Tagant-Richat-Tiris Trough; Bronner, 1992; Villeneuve and Cornée, 1994; Matton, 2008) sub-parallel to the elongation axis of the caldera. This major structural anisotropy was therefore favourably oriented for tensional reactivation and to have controlled the development of the magma chamber and the overlying caldera. The values of ellipticity measured in the Richat (0.87-0.88) also agree with analogue modelling experiments where collapse calderas controlled by pre-existing discontinuities displayed ellipticity values between 0.8 and 0.9 (Acocella et al., 2004). It is thus likely that the NE-SW elongation of the Richat caldera be the surface expression of the reactivation of the pre-existing Tagant-Richat-Tiris Trough.

7.2 Structural implications

The Richat complex appears to be characterized by the overprinting of two structural systems: (1) a regional system defined by old regional fracture networks, mostly oriented NNE-SSW and ENE-WSW (Bayer and Lesquer, 1978; Netto et al., 1992; Poupeau et al., 1996) and (2) a local, doming-related, fractures set. Close relationships between magmatism and these two systems may also be defined. The undersaturated rocks (carbonatites and kimberlite) are controlled by the regional fracture set, filling NNE-SSW dextral strike-slip faults and en-echelon tension gashes. On the other hand, the bimodal

suite is controlled by the local stress regime as shown by the concentric gabbroic dikes, probably related to annular fracturing, and the rhyolites restricted to a central piston-like collapse.

The relationship between structures and magma types is directly related to the emplacement processes and generation depth of the magmas. For the bimodal suite, eruptions were controlled by the underlying magma chamber and shallow mechanisms of caldera collapse and resurgence, Gabbroic magmas may have followed the same regional weaknesses to rise into the crust before the formation of the magma chamber at a shallow level. Carbonatites/kimberlite emplacement followed deep structural weaknesses that acted as pathways for magma ascent through the lithosphere (Woolley and Bailey, 2012). Their orientation is similar to the overall elongation of the caldera.

7.3 Emplacement history

Taking into account the petrological, structural, geochemical, geophysical and field data, the following stages of emplacement history are proposed (Fig. 12):

Stage 1 (shortly before 100 Ma): Magma derived from the sub-continental lithospheric mantle rises in the crust, following pre-existing anisotropies, and produces doming and propagation of ring and radial fractures. A magma chamber is created and is affected by upper crustal contamination. Increasing pressure in the magma chamber results in eruptions of basaltic magmas along concentric fractures to form the gabbroic ring dikes.

Stage 2 (~100 Ma): Reactivation of the pre-existent aulacogenous structure at deep lithospheric levels allows rapid ascension of kimberlitic and carbonatitic magmas,

crosscutting previous gabbroic ring dikes, in connection with caldera subsidence (Anderson et al., 2013). Fusion of the crust and magma differentiation is initiated. Hydrothermal fluids are produced from the magma chamber and canalized into the intensely fractured and permeable central zone created by the doming. Dissolution of the limestone unit leads to hydrothermal karst-collapse megabreccia..

Stage 3 (shortly after 100 Ma): Rhyolitic magmatism rises up along the conical fractures and erupts in violent explosions, probably due to interaction with caldera-lake water. Reopening of ring fractures associated with felsic volcanism led to piston-like collapse along circular fractures.

Stage 4 (post volcanic to present day): Erosion creates circular ridges represented by nested quartzitic sandstone rings while collapsed central extrusive felsic facies and hydrothermal karst infilling are preserved (Fig. 13).

8. Conclusion

The nature and significance of the rocks from the Richat complex has been the subject of prolonged debate and interrogation. Several studies focussed on the description and the understanding of the central breccia, the “analcimolites”, the gabbroic rocks or the carbonatites but previous studies have never led to a global understanding of these rocks and the establishment of their possible relationships into a comprehensive model.

In this paper, we showed that the Richat complex is composed of a bimodal tholeiitic suite crosscut by undersaturated carbonatitic and kimberlitic dikes and sills. The bimodal suite is characterized by two concentric gabbroic ring dikes and two extrusive rhyolitic centers.

Gabbroic rocks are not part of the Triassic-Jurassic tholeiitic event (CAMP) as previously thought, but confine to the Cretaceous Richat structure. However, a similar metasomatized sub-continental lithospheric mantle source, but more affected by upper crustal contamination, is likely for the origin of the Richat mafic igneous rocks. The remarkable geochemical compatibility with Low-Ti CAMP basalts of West Africa and the fact that both eruptions (CAMP and Richat emplacement) are separated by ~100 Ma also preclude deep plume intervention in the genesis of the Richat.

The extrusive rhyolitic centers represent the remnant of two volcanic craters aligned along a NE-SW trend, in the elongation axis of the caldera. Previously described as “analcimolites” these rocks appear to be rhyolites and rhyolitic tuffs, altered by low temperature hydrothermal solutions.

Hydrothermalism played an important role in the evolution of the Richat complex. It is responsible, notably, for the karst-collapse central megabreccia formation, the alteration sequence of the rhyolites, the potassic alteration of the gabbros and the stable isotope enrichment in the carbonatites. All that happened most probably at about 99 Ma.

Coexistence of intrusive alkaline and tholeiitic rocks within the same igneous complex shows the importance of the regional structural system on the caldera history. Pre-existing deep structural weaknesses responsible for the elliptical shape of the Richat caldera acted as a pathway for the ascent of magmas and allowed the rise of carbonatitic and kimberlitic melts from the asthenosphere, and basaltic magma from the sub-continental lithospheric mantle. At subsurface levels, eruption of the tholeiitic suite was controlled by the underlying magmatic chamber and shallow mechanisms of caldera

collapse and resurgence, whereas the carbonatites/kimberlite magmas were emplaced along the old regional anisotropies.

The Richat complex thus provides a rare exposure of magma collected at several distinct depths. Chronology of the magmatic phases suggests a downward propagation of a permeable zone under tensional intra-plate stresses. More dating is required to better constrain the evolution of this exceptional geological object. Direction of vertical propagation during reactivation of lithospheric anisotropies should be more precisely tested with analogue modelling or age dating on complexes providing magmas from different depths.

Acknowledgements

We thank C. Verati for precious CAMP data, Pierre-Simon Ross for his comments, André Michard and Mohamed Bouabdellah for their constructive reviews, and Michelle Laithier for her help with the figures. This work was supported by a grant from the Natural Sciences and Engineering Research Council of Canada (NSERC) to Matton, and an NSERC Discovery grant to Jébrak.

References

- Abdelsalam, M.G., Gao, S.S., and Liégeois, J.P., 2011. Upper mantle structure of the Saharan Metacraton. *J. Afr. Earth Sci.* 60, 328-336.
- Acocella, V., 2007. Understanding caldera structure and development: An overview of analogue models compared to natural calderas. *Earth-Science Reviews* 85,125–160.
- Acocella, V., Funicello, R., Marotta, E., Orsi, G., and de Vita, S., 2004. The role of extensional structures on experimental calderas and resurgence. *J. Volcanol. Geotherm. Res.* 129, 199-217.
- Andersson, M., Malehmir, A., Troll, V.R., Dehghannejad, M., Juhlin, C., and Ask, M. 2013. Carbonatite ring-complexes explained by caldera-style volcanism. *Nature Scientific Report* 1677, 14 p.
- Bardossy, G., Monod, T., and Pomerol, C., 1963. Decouverte d'analcimolites d'origine endogene dans les Richat (Adrar mauritanien). *C. R. Acad. Sci.* 256, 3934-3936.
- Bayer, M. and Lesquer, A., 1978. Les anomalies gravimétriques de la bordure orientale du craton Ouest-africain. *Géométrie d'une suture panafricaine. Bull. Soc. Géol. Fr.* 7, 863-876.
- Berrahma, M. and Delaloye, M., 1989. Données géochronologiques nouvelles sur le massif volcanique du Siroua (Anti-Atlas Morocco). *J. Afr. Earth Sci.* 9, 651-656.
- Blanc, P. and Pomerol, C., 1973. Étude pétrographique des roches magmatiques, des filons carbonatés et des analcimolites des Richat. In: Monod, T., Pomerol, C., (Eds.), *Contributions à l'étude de l'accident circulaire des Richat (Adrar de Mauritanie). Sci. Terre Mem.* 28, Nancy, pp. 107-121.

- 636 Bosworth, W., Burke, K., and Strecker, M., 2000. Magma chamber elongation as an indicator of
637 intraplate stress field orientation; 'borehole breakout mechanism' and examples from the
638 late Pleistocene to Recent Kenya Rift valley. In: Jessell, M.W., Urai, J. L., (Eds.), Stress,
639 strain and structure; a volume in honor of W. D. Means. Journal of the Virtual Explorer
640 online, v. 2.
- 641 Bouabdellah, M., Hoernle, K., Kchit, A., Duggen, S., Hauff, F., Klügel, A., D. Lowry &
642 Beaudoin, G. 2010. Petrogenesis of the Eocene Tamazert continental carbonatites
643 (Central High Atlas, Morocco): implications for a common source for the Tamazert and
644 Canary and Cape Verde islands carbonatites. Journal of Petrology, 51, 1655-1686.
- 645 Boussaroque, J. L., 1975. Étude des analcimolites des Richat (Adrar de Mauritanie) [Ph.D.
646 thesis]. Univ. Paris VI, Paris, 105 p.
- 647 Bronner, G., 1992. Structure et évolution d'un craton archéen: La dorsale Réguibat occidentale
648 (Mauritanie); tectonique et métallogénie des formations ferrifères. Éditions du Bureau de
649 Recherches Géologiques et Minières, 448 p.
- 650 Cailleux, A., Guillemaut, A., and Pomerol, C., 1964. Présence de coésite, indice de hautes
651 pressions, dans l'accident circulaire des Richat (Adrar mauritanien). C. R. hebd. séanc.
652 Acad. Sci. 258, 5488-5490.
- 653 Carmichael, I. S. E., 1964. The petrology of Thingmuli, a Tertiary volcano in eastern Iceland. J.
654 Petrol. 5, 435-460.
- 655
- 656 Castorina, F., Censi, P., Comin-Chiaramonti, P., Piccirillo, E. M., Alcover Neto, A., Gomes, C.
657 B., Ribeiro de Almeida, T. I., Speziale, S., and Toledo, M. C. M., 1997. Carbonatites
658 from eastern Paraguay and genetic relationships with potassic magmatism; C, O, Sr and

- 659 Nd isotopes. *Min. Petrol.* 61, 237-260.
- 660 Cox, K. G. and Hawkesworth, C. J., 1985. Geochemical stratigraphy of the Deccan Traps at
661 Mahabaleshwar, western Ghats, India, with implications for open system magmatic
662 processes. *J. Petrol.* 26, 355-377.
- 663 Dani, N., Formoso, M. L. L., Decarreau, A., and Meunier, A., 2001. Nordstrandite in bauxite
664 derived from phonolite, Lages, Santa Catarina, Brazil. *Clays and Clay Minerals* 49, 216-
665 226.
- 666 De Min, A., Piccirillo, E. M., Marzoli, A., Bellieni, G., Renne, P. R., Ernesto, M., and Marques,
667 L. S., 2003. The Central Atlantic Magmatic Province (CAMP) in Brazil-petrology,
668 geochemistry, $^{40}\text{Ar}/^{39}\text{Ar}$ ages, paleomagnetism and geodynamic implications. In: Hames,
669 W. E., McHone, J. G., Renne, P. R., Ruppel, C., (Eds), *The Central Atlantic Magmatic
670 Province: Insights from Fragments of Pangea*. AGU, Geophysical Monograph 136, pp.
671 91-128.
- 672 Deckart, K., Bertrand, H., and Liegeois, J.-P., 2005. Geochemistry and Sr, Nd, Pb isotopic
673 composition of the Central Atlantic Magmatic Province (CAMP) in Guyana and Guinea.
674 *Lithos* 82, 289-314.
- 675 Deines, P., 1989. Stable isotope variations in carbonatites. In: Bell, K., (Ed), *Carbonatites;
676 genesis and evolution*. Unwin Hyman, London, U. K., pp. 301-359.
- 677 Destombes, J.-P. and Plote, H., 1962. Une structure aberrante dans le Précambrien du Sahara
678 mauritanien; hypothèse nouvelle sur l'origine du Richat (Adrar mauritanien). *C. R. somm.
679 Soc. Géol. Fr.* 7, 202-203.
- 680 Dietz, R. S., Fudali, R., and Cassidy, W., 1969. Richat and Semsiyat domes (Mauritania); not

- 681 astroblemes. Geol. Soc. Am. Bull. 80, 1367-1372.
- 682 Eby, G. N., 1975. Abundance and distribution of the rare-earth elements and yttrium in the rocks
683 and minerals of the Oka carbonatite complex, Quebec. *Geochimica et Cosmochimica*
684 *Acta* 39, 597-620.
- 685 Fabre, J., 1999. Quinze jours avec Théodore Monod, *Eurêka* 41, 36-47.
- 686 Fudali, R. F., 1973. Origin of the analcime-bearing rocks of Richat, In: Monod, T., Pomerol, C.,
687 (Eds.), *Contributions à l'étude de l'accident circulaire des Richat (Adrar de Mauritanie)*.
688 *Sci. Terre Mem.* 28, Nancy, pp. 97-105.
- 689 Gupta, A. K. and Fyfe, W. S., 1975. Leucite survival; the alteration to analcime. *Can. Min.* 13,
690 361-363.
- 691 Heatherington, A. L. and Mueller, P. A., 1999. Lithospheric sources of North Florida, USA
692 tholeiites and implications for the origin of the Suwannee Terrane. *Lithos* 46, 215-233.
- 693 Irvine, T. N. and Baragar, W. R. A., 1971. A guide to the chemical classification of the common
694 volcanic rocks. *Can. J. Earth Sci.* 8, 523-548.
- 695 Jesus, M.F., Fernando, R.P., Paz, M.P.M., Delgado, H. A., Teresa, S.F.M., Francisco, G.T.,
696 Fernando, L.V., Antonio, R. L.J. and Menor, S.C. 2011. Multianalytical characterization
697 of silica-rich megabreccias from the proposed natural area of Richat (Sahara desert,
698 Mauritania). *Research Journal of Chemistry and Environment* 15, 49–54.
- 699 Jourdan, F., Marzoli, A., Bertrand, H., Cosca, M., and Fontignie, D., 2003. The northernmost
700 CAMP; $^{40}\text{Ar}/^{39}\text{Ar}$ age, petrology and Sr-Nd-Pb isotope geochemistry of the Kerforne
701 Dike, Brittany, France, In: Hames, W. E., McHone, J. G., Renne, P. R., Ruppel, C., (Eds),
702 *The Central Atlantic Magmatic Province: Insights from Fragments of Pangea*. AGU,

- 703 Geophysical Monograph 136, 209-226.
- 704 Keller, J. and Hoefs, J., 1995. Stable isotope characteristics of natrocarbonatites from Oldoinyo
- 705 Lengai. In: Bell, K., Keller, J., (Eds), Carbonatite Volcanism: Oldoinyo Lengai and the
- 706 Petrogenesis of Natrocarbonatites. IAVCEI Proc. Volc. 4, pp. 113–123.
- 707 Kresten, P., 1980. The Alnö complex: tectonics of dyke emplacement. Lithos, 13: 153-158.
- 708 Le Bas, M. J., Le Maitre, R. W., Streckeisen, A., and Zanettin, B. A., 1986. Chemical
- 709 classification of volcanic rocks based on the total alkali-silica diagram. J. Petrol. 27, 745-
- 710 750.
- 711 Loubet, M., Bernat, M., Javoy, M., and Allegre, C. J., 1972. Rare earth contents in carbonatites.
- 712 Earth Planet. Sci. Lett. 14, 226-232.
- 713 Mariano, A. N., 1989. Nature of economic mineralisation in carbonatites and related rocks. In:
- 714 Bell, K., (Ed.), Carbonatites; genesis and evolution. Unwin Hyman, London, U. K., pp.
- 715 149-176.
- 716 Matton, G., 2008, La structure du Richat (Mauritanie), un processus alcalin péri-Atlantique, Ph.D,
- 717 Université du Québec à Montréal, 173 p.
- 718 Matton, G. and Jébrak, M., 2009. The Cretaceous Peri-Atlantic Alkaline Pulse (PAAP): deep
- 719 mantle plume origin or shallow lithospheric break-up ? Tectonophysics 469: 1-12.
- 720 Matton, G., Jébrak, M., and Lee, J. K. W., 2005. Resolving the Richat enigma: Doming and
- 721 hydrothermal karstification above an alkaline complex. Geology 33, 665-668.
- 722 McDonough, W. F., Sun, S. S., Ringwood, A. E., Jagoutz, E., and Hofmann, A. W., 1992.
- 723 Potassium, rubidium, and cesium in the Earth and Moon and the evolution of the mantle

- 724 of the Earth. *Geochim. Cosmoch. Acta* 56, 1001-1012.
- 725 Michard, A., Soulaïmani, A., Hoepffner, C., Ouanaimi, H., Baidder, L., Rijmati, E.C., Saddiqi,
 726 O., 2010. The South-Western branch of the Variscan Belt: Evidence from Morocco.
 727 *Tectonophysics* 492: 1-24.
- 728 Mitchell, R. H., 1995. Kimberlites, orangeites, and related rocks. Plenum Press, New York, USA,
 729 pp. 410.
- 730 NASA/GSFC/METI/ERSDAC/JAROS and U.S./Japan ASTER Science Team, "Richat Structure,
 731 Oudane, Mauritania", ASTER Image acquired October 7, 2000.
 732 <http://asterweb.jpl.nasa.gov/gallery-detail.asp?name=Richat>.
- 733
- 734 Netto, A. M., Fabre, J., Poupeau, G., and Champemmois, M., 1992. Datations par traces de
 735 fissions de la structure circulaire des Richats. *C. R. Acad. Sci.* 314, 1179-1186.
- 736 Olson, J.C., and Hedlund, D.C., 1981. Alkalic rocks and resources of thorium and associated
 737 elements in the Powderhorn district, Gunnison Country, Colorado. A review of thorium
 738 resources, their distribution, and geologic relationships. Geological Survey Professional
 739 Paper 1049-C, 34 p.
- 740 Onuonga, I. O., Fallick, A. E., and Bowden, P., 1997. The recognition of meteoric-hydrothermal
 741 and supergene processes in volcanic carbonatites, Nyanza Rift, western Kenya, using
 742 carbon and oxygen isotopes. *J. Afr. Earth Sci.* 25, 103-113.
- 743 Pearce, J. A., 1983. Role of sub-continental lithosphere in magma genesis in active continental
 744 margins. In: Hawkesworth, C.J., Norry, M.J., (Eds.), *Continental basalts and mantle*
 745 *xenoliths*, Shiva, Amsterdam, pp. 230–249.

- 746 Pegram, W. J., 1990. Development of continental lithospheric mantle as reflected in the chemistry
747 of the Mesozoic Appalachian tholeiites, U.S.A. *Earth Planet. Sci. Lett.* 97, 316-331.
- 748 Poupeau, G., Fabre, J., Labrin, E., Azdimoussa, A., Netto, A. M., and Monod, T., 1996.
749 Nouvelles datations par traces de fission de la structure circulaire des Richat
750 (Mauritanie). *Mém. Serv. Géol. Alg.* 8, 231-236.
- 751 Reid, D. L. and Cooper, A. F., 1992. Oxygen and carbon isotope patterns in the Dicker Willem
752 carbonatite complex, southern Namibia. *Chem. Geol.* 94, 2293-2405.
- 753 Rooney, A.D., Selby, D., Houzay, J.P., Renne, P.R., 2010. Re-Os geochronology of a
754 Mesoproterozoic sedimentary succession, Taoudeni basin, Mauritania: Implications for
755 basin-wide correlations and Re-Os organic-rich sediments systematics, *Earth Planet. Sci.*
756 *Lett.* 289 (3-4), 486-496.
- 757 Stachel, T., Lorenz, V., Stanistreet, I.G. 1994., Gross Brukkaros (Namibia) – an enigmatic crater-
758 fill reinterpreted as due to Cretaceous caldera evolution. *Bull. Volcanol.* 56: 386-397.
- 759 Sun, S. S. and McDonough, W. F., 1989. Chemical and isotopic systematics of oceanic basalts;
760 implications for mantle composition and processes. In: Saunders, A. D., Norry, M. J.,
761 (Eds.), *Magmatism in the ocean basins*, *Geol. Soc. Spec. Publ.* 42, 313-345.
- 762 Taylor, S. R. and McLennan, S. M., 1995. The geochemical evolution of the continental crust.
763 *Rev. Geophys.* 33, 241-265.
- 764 Trompette, R., 1973a. Les dolérites de l'Adrar de Mauritanie et le problème des analcimolites des
765 Richat. In : Monod, T., Pomerol, C., (Eds.), *Contributions à l'étude de l'accident*
766 *circulaire des Richat (Adrar de Mauritanie)*. *Sci. Terre Mem. Nancy* 28, 83-95.
- 767 Trompette, R., 1973b. Le Précambrien supérieur et le Paléozoïque inférieur de l'Adrar de

- 768 Mauritanie: Bordure occidentale du bassin de Taoudenni, Afrique de l'ouest [Ph.D.
769 thesis]. Université de Saint Jérôme, Marseille, 573 p.
- 770 Verati, C., Bertrand, H., and Feraud, G., 2005. The farthest record of the Central Atlantic
771 magmatic province into West Africa Craton; precise $^{40}\text{Ar}/^{39}\text{Ar}$ dating and geochemistry
772 of Taoudenni Basin intrusives (northern Mali). *Earth Planet. Sci. Lett.* 235, 391-407.
- 773 Weaver, B. L. and Tarney, J., 1981. Lewisian gneiss geochemistry and Archaean crustal
774 development models. *Earth Planet. Sci. Lett.* 55, 171-180.
- 775 Villeneuve, M., 2008. Review of the orogenic belts on the western side of the West African
776 Craton: the Bassarides, Rokelides and Mauritanides. In: Ennih, N. and Liégeois, J.P.
777 (eds.) *The boundaries of the West African craton*. Geol. Soc. Spec. Publ. 297, 169-201.
- 778 Villeneuve, M. and Cornée, J. J., 1994. Structure, evolution and palaeogeography of the West
779 African Craton and bordering belts during the Neoproterozoic. *Prec. Res.* 69, 307-326.
- 780 Wilson, M., 1989. *Igneous petrogenesis; a global tectonic approach*, Unwin Hyman, London, U.
781 K., 466 p.
- 782 Wilson, M. and Downes, H., 2006. Tertiary-Quaternary intra-plate magmatism in Europe and its
783 relationship to mantle dynamics. In: Gee, D.G. and Stephenson, R. (eds.) *European*
784 *lithosphere dynamics*. Geological Society of London Memoir 32. London: Geological
785 Society of London, pp. 147-166.
- 786 Woolley, A. R. and Kempe D.R.C., 1989. Carbonatites: nomenclature, average chemical
787 compositions and element distribution. In: Bell, K., (Ed.), *Carbonatites; genesis and*
788 *evolution*, Unwin Hyman, London, U. K., pp. 1-14.
- 789 Woolley, A. R. and Bailey, D. K., 2012. The crucial role of lithospheric structure in the

generation and release of carbonatites: geological evidence. *Mineralogical Magazine* 76:
259-270.

Woolley, A. R., Rankin, A. H., Elliott, C. J., Bishot, A. C., and Niblett, D., 1984. Carbonatite
dykes from the Richat dome, Mauritania, and the genesis of the dome. *The Indian Min.*
189-207.

Figure captions

Figure 1. A: Location map for Richat dome. Taoudenni Basin is shaded; (M)
Mauritanides. B: Modified satellite image of Richat structure after NASA and U.S./Japan
ASTER Science Team, 2000. ENE-WSW faults display sinistral movement as shown by
offset of external ridge (white arrows). Dashed lines represent major faults and fractures;
dot-stippled lines, endorheic fluvial streams. The irregular patch in the southwestern
central area is the locus of a sebkha. Schematic map displaying distribution of magmatic
phases: volcanic craters (crosses), high-K gabbro (star), kimberlitic plug and sills
(diamond) and carbonatite dikes (dot-stippled lines). C: Magnetic survey of the Richat
structure showing the kimberlitic plug (northern part) and the gabbroic ring dykes. Note
the gap in the southwestern part of the inner gabbroic dike due to the maar system and the
displacement of the external gabbroic ring dike by the NNE-SSW fault system in the
northeastern part of the map. Magnetic survey courtesy of Ashton Mining Inc. D: Central
part of Richat structure. Rhyolitic volcanic basins (crosses) and associated diatremes
outcrop to SW and NE of breccia (triangles). Internal gabbroic ring dike (thick black
lines) only outcrops in the eastern central part of the Richat. Circular faulting appears in
dashed lines. Ring faults are inferred from stratigraphic considerations, repetitions of
geological units, satellite imagery and from previous work (Monod and Pomerol, 1973;

Boussaroque, 1975). The inner circular ridge is composed of sandstone and represented by a grey pattern.

Figure 2. Photographs of different features from the volcanic rocks of the Richat dome. Scale bar is calibrated in cm. A: Hand specimen of the basal ejecta layer from the southwestern crater rim. B: View looking southwest of the northeastern crater. Dashed line highlights the central depression. C: Sharp contact between the brecciated-conglomeratic unit and the overlying massive quartz-phyric rhyolite (unit 2) at the northeastern crater rim. D: Hand specimen showing the “egg-shell” texture (center) and the analcime glomerocrysts-rich unit (glomerocrysts appear in cream - light beige color on the picture; unit 3). E: Vesicles-rich specimen from the upper part of unit 3. F: Outcrop showing diffusion structures in unit 4. G: Large lithophysae characterize the summital unit. H: The core of the Richat structure is occupied by the high-relief karst-collapse siliceous megabreccia. Dashed line shows emerging breccia body from the sand. Tent in foreground for scale.

Figure 3. Stratigraphy of volcanic units. 1a: ejecta, 1b: breccia to conglomeratic facies, 2: porphyritic quartz rhyolite, 3: “glomerules-supported” unit with vesicles increasing in size and quantity from base to top, 4: lithophysae facies.

Figure 4. Photomicrographs of features from different Richat lithologies. A: Glomerocrysts of analcime characterized by a core of analcime and a rim of nordstrandite interlaced with analcime. XPL. B: Quartz crystals corroded by calcite in rhyolites. The

groundmass is highly anisotropic due to analcime content. XPL. C: Interstitial filling and veinlet of analcime and iron oxide in rhyolite. Remnants of calcite are present. XPL. D: Coarse-grained cavity filling of euhedral analcime. PPL. E: Calcite crystals corroded by analcime in highly altered rhyolites. XPL. F: Quartz crystals corroded by analcime in rhyolites. XPL. G: Secondary neoformed K-feldspar along veinlet wall in altered gabbros. XPL. H: Ophitic texture of the gabbros. Note the lath-shaped sub-euhedral plagioclase crystals with interstitial pyroxene. XPL. I: Lath-shaped plagioclase crystal corroded by sericitized k-feldspars in altered gabbros. XPL. Abbreviations: (An) analcime; (No) nordstrandite; (Qz) quartz; (Cc) Calcite; (K-Feld) K-feldspar; (Pl) Plagioclase; (PPL) Plane-polarized light; (XPL) Cross-polarized light.

Figure 5. A: Total alkali-silica classification diagram for mafic (squares) to felsic (diamonds) rocks from the Richat complex (after Le Bas et al., 1986). Solid line and dashed lines represent magmatic series and alteration sequences respectively. B: AFM diagram for unaltered gabbros and the freshest rhyolites. Also shown are lava compositions and trends (faint lines) for a typical tholeiitic sequence (Thingmuli volcano, Iceland – shown as filled circles – from Carmichael, 1964) and a typical calc-alkaline trend (the average composition of Cascades lavas – shown as open rings – from Carmichael, 1964). The boundary between the calc-alkaline field and the tholeiitic field (thick black line) is from Irvine and Baragar (1971). FeO^* : $\text{FeO} + \text{Fe}_2\text{O}_3$.

Figure 6. Geochemical plots of volcanic rocks showing CaO , Na_2O and Al_2O_3 against SiO_2 . Increasing levels of alteration are shown by decreasing SiO_2 .

Figure 7. Trace element plots for Richat ring dikes, normalized to (A) Mid-Ocean Ridge Basalts (after Sun and McDonough, 1989) and (B) Ocean Island Tholeiites (after Thompson et al., 1984), respectively. Arrows indicate main enrichments and depletions relative to the ocean-island tholeiites. C: Primitive mantle normalized multi-element diagrams for Richat tholeiites and average amphibolites (upper crust) and granulites (lower crust) (after Weaver and Tarney, 1981). D: Primitive mantle-normalized (after McDonough et al., 1992) multi-element diagrams for Richat tholeiites and CAMP representatives from West Africa (Taoudenni dikes and sills from Mali after Verati et al., 2005 and tholeiitic samples from Guinea after Deckart et al., 2005).

Figure 8. Th/Yb vs Ta/Yb diagram (after Pearce, 1983 and inspired from Wilson, 1989) for Richat gabbros. Vectors shown indicate the influence of subduction components (S), crustal contamination (C), within-plate enrichment (W) and fractional cristallisation (F). UC: Upper crustal composition after Weaver and Tarney (1981). Uncontaminated intracontinental plate basalts should plot in the enriched mantle region (Wilson, 1989). Dashed line arrow indicates possible path of Richat gabbros contamination by the upper crust.

Figure 9. Harker diagrams for gabbros and rhyolites from the Richat complex. Gabbros are represented by squares whereas freshest rhyolites define the dashed line area. Compatible and incompatible trace elements versus SiO₂ for gabbros and rhyolites from the Richat complex.

Figure 10. Rare earth elements (REE) normalized to chondritic composition (Sun and McDonough, 1989) for of (A) gabbros and rhyolites and (B) kimberlites and carbonatites.

The shaded carbonatite field (pale grey – dashed line) is based on data from Loubet et al. (1972) and Eby (1975) and the shaded field of kimberlites (dark grey) is from Mitchell (1995). Carbonatites are represented by open triangles, kimberlite by solid triangles. (C) Chemical classification of carbonatites using wt % oxides (after Woolley and Kempe, 1989). Abbreviations: (Cc) Calcio-carbonatite; (Mc) Magnesio-carbonatite; (Fc) Ferro-carbonatite. FeO*: FeO+Fe₂O₃

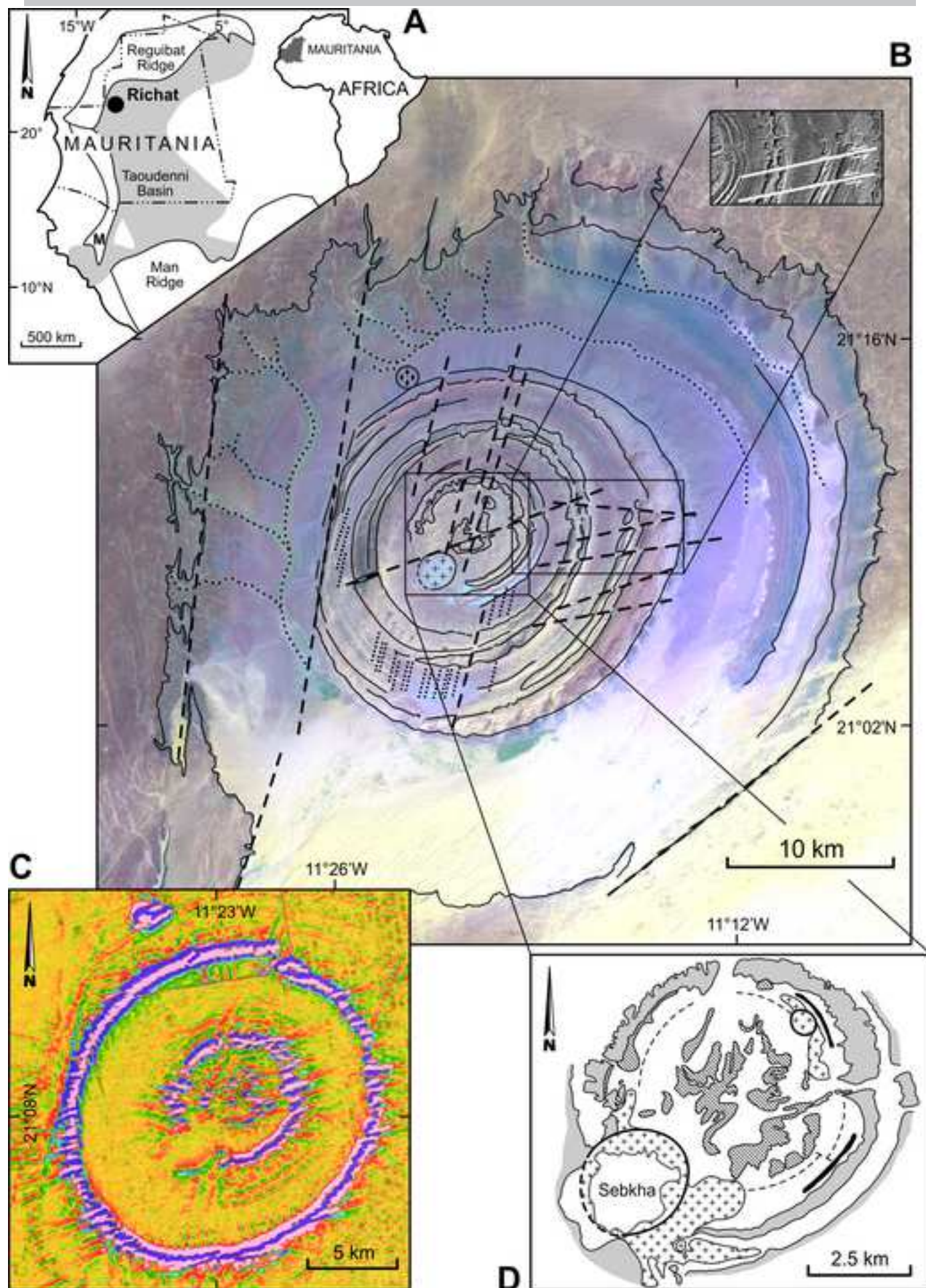
Figure 11. Plot of $\delta^{13}\text{C}$ vs $\delta^{18}\text{O}$ composition of carbonatite dikes from the Richat dome. PIC: box of primary igneous carbonatites (Deines, 1989).

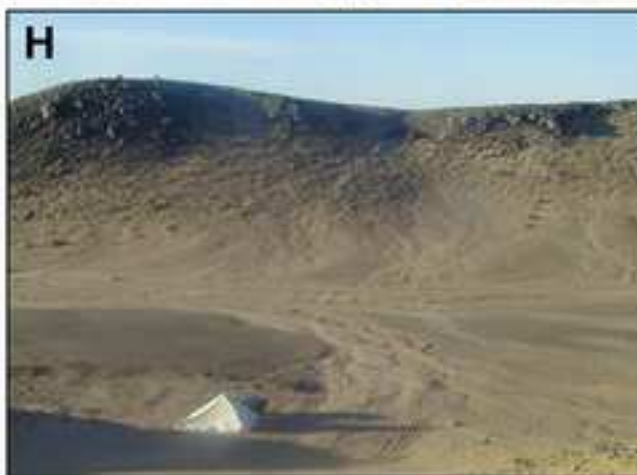
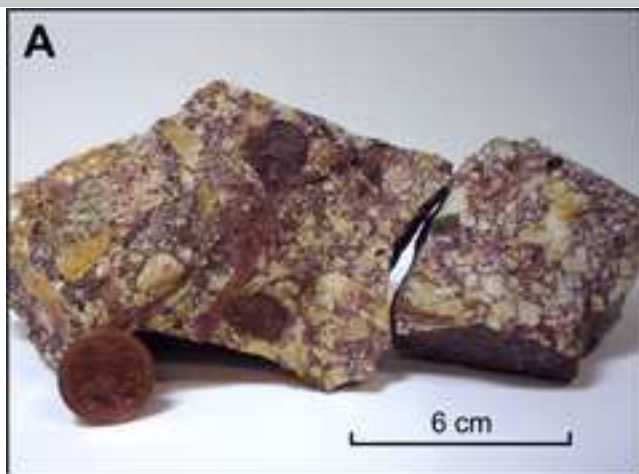
Figure 12. Emplacement history of the Richat complex. See text for explanation.

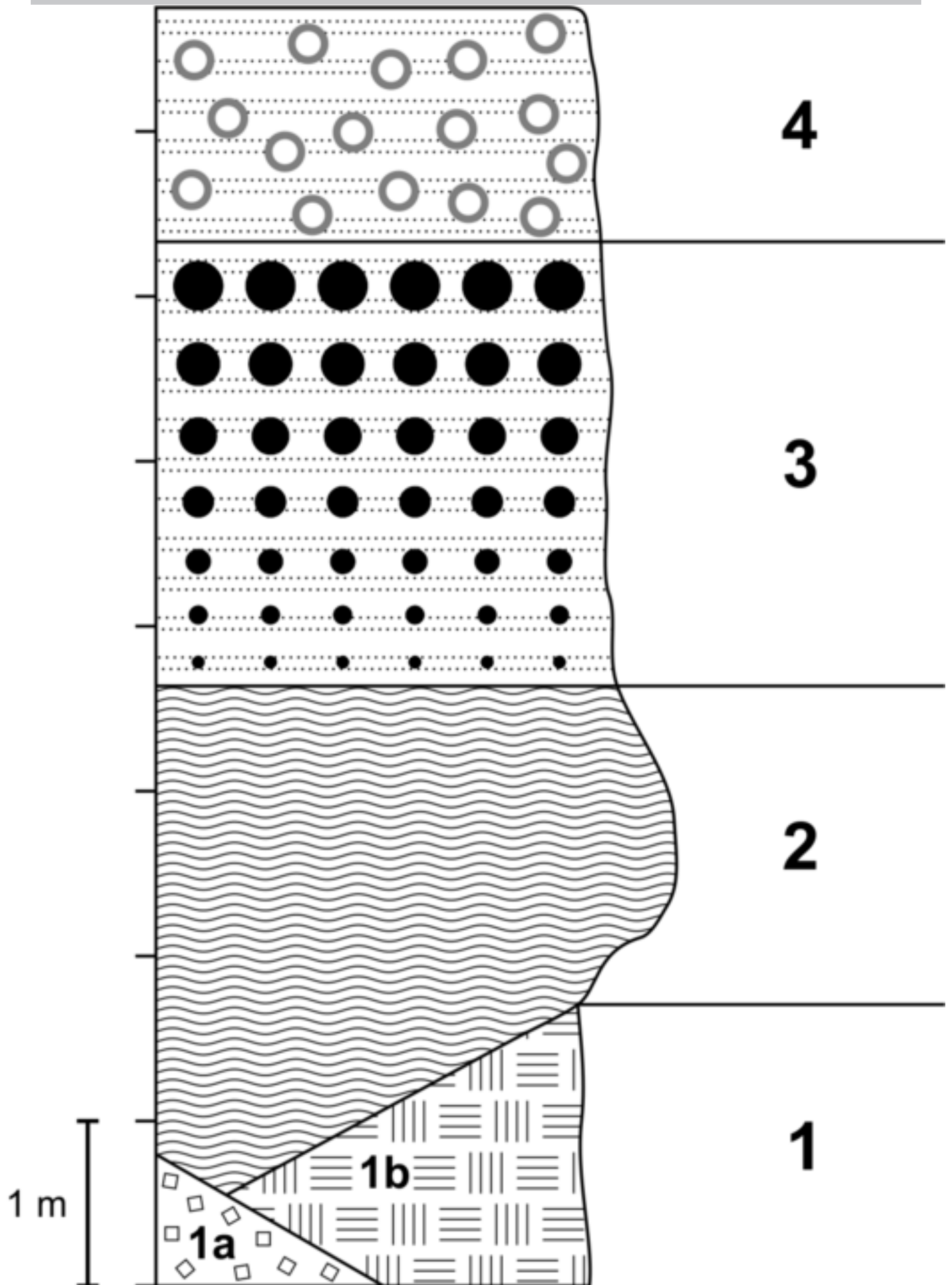
Figure 13. Perspective view of the Richat complex with the possible shape of the magmatic chamber, inspired by Stachel et al. (1994) and Andersson et al. (2013).

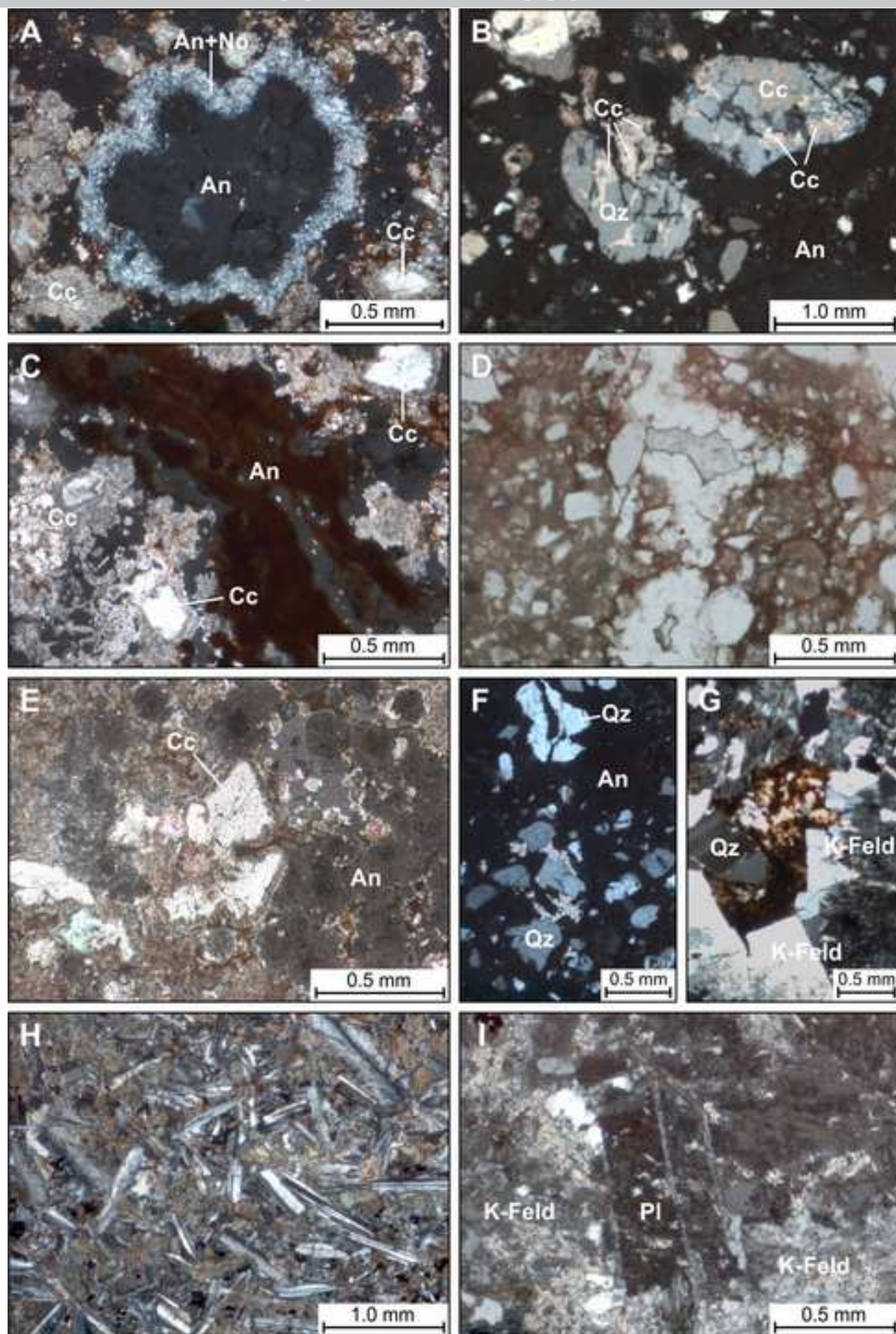
Table 1. Paragenetic mineral sequence of volcanic rocks of the Richat complex. Tr = trace. Initial volcanic rocks represent the primary assemblage whereas the actual outcropping volcanic rocks represent the secondary assemblage.

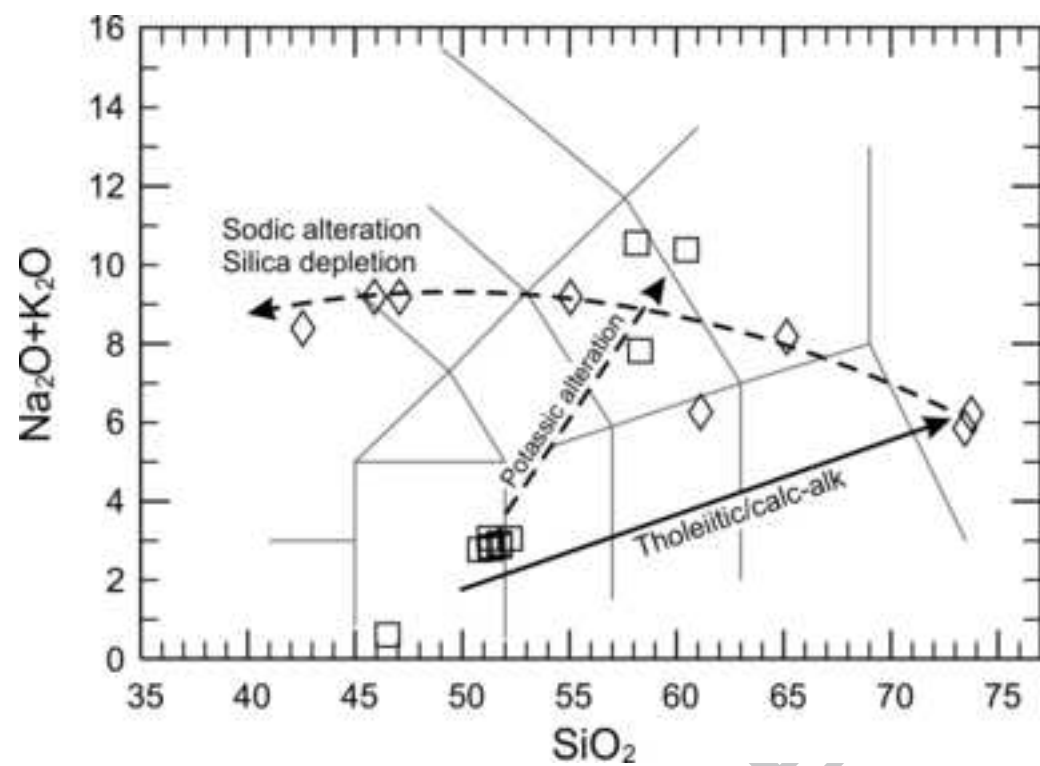
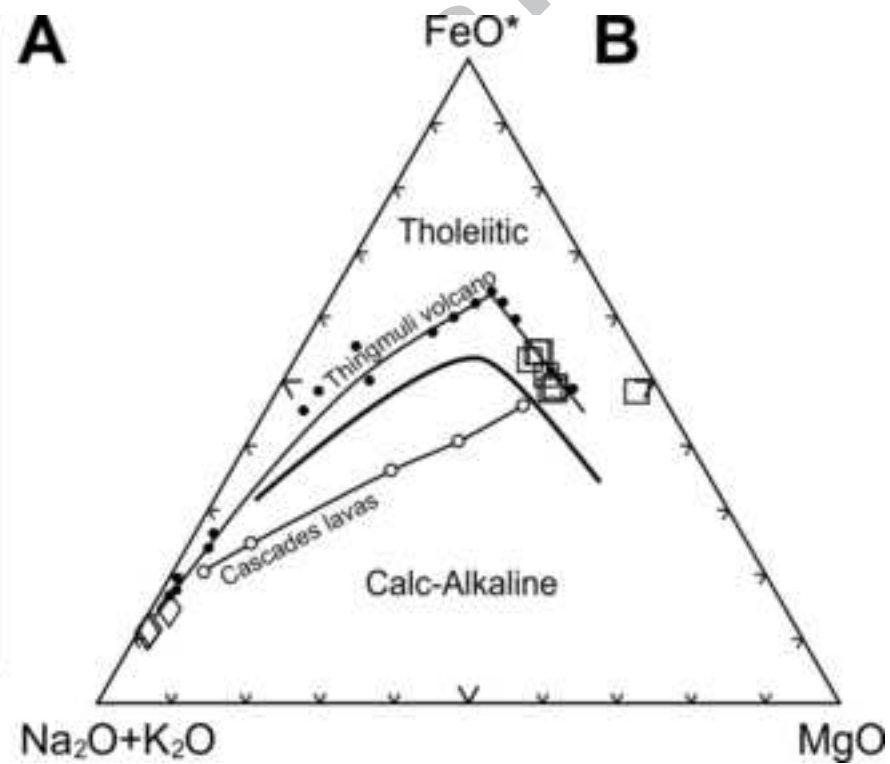
Table 2. Geochemical results for major and traces elements

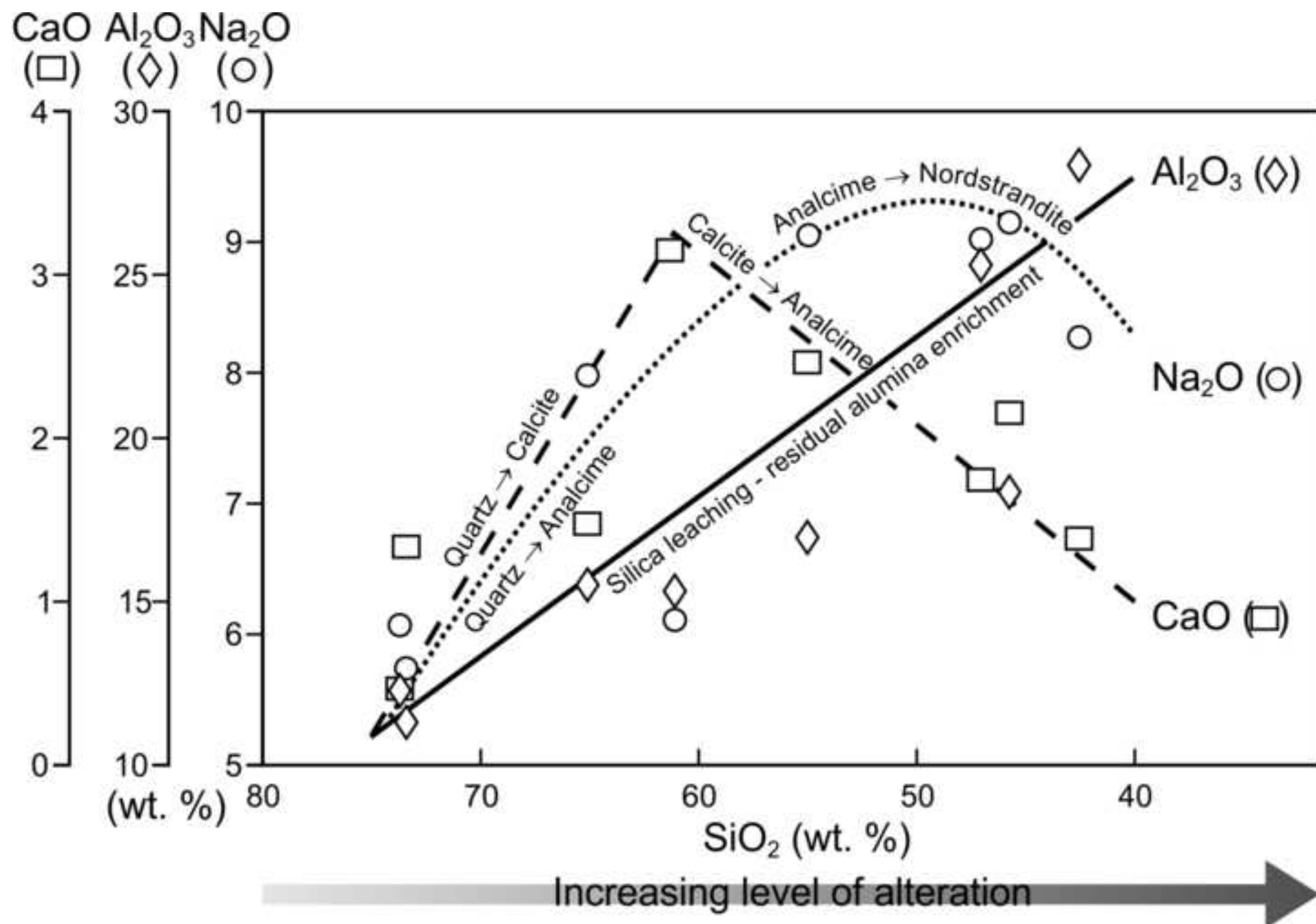


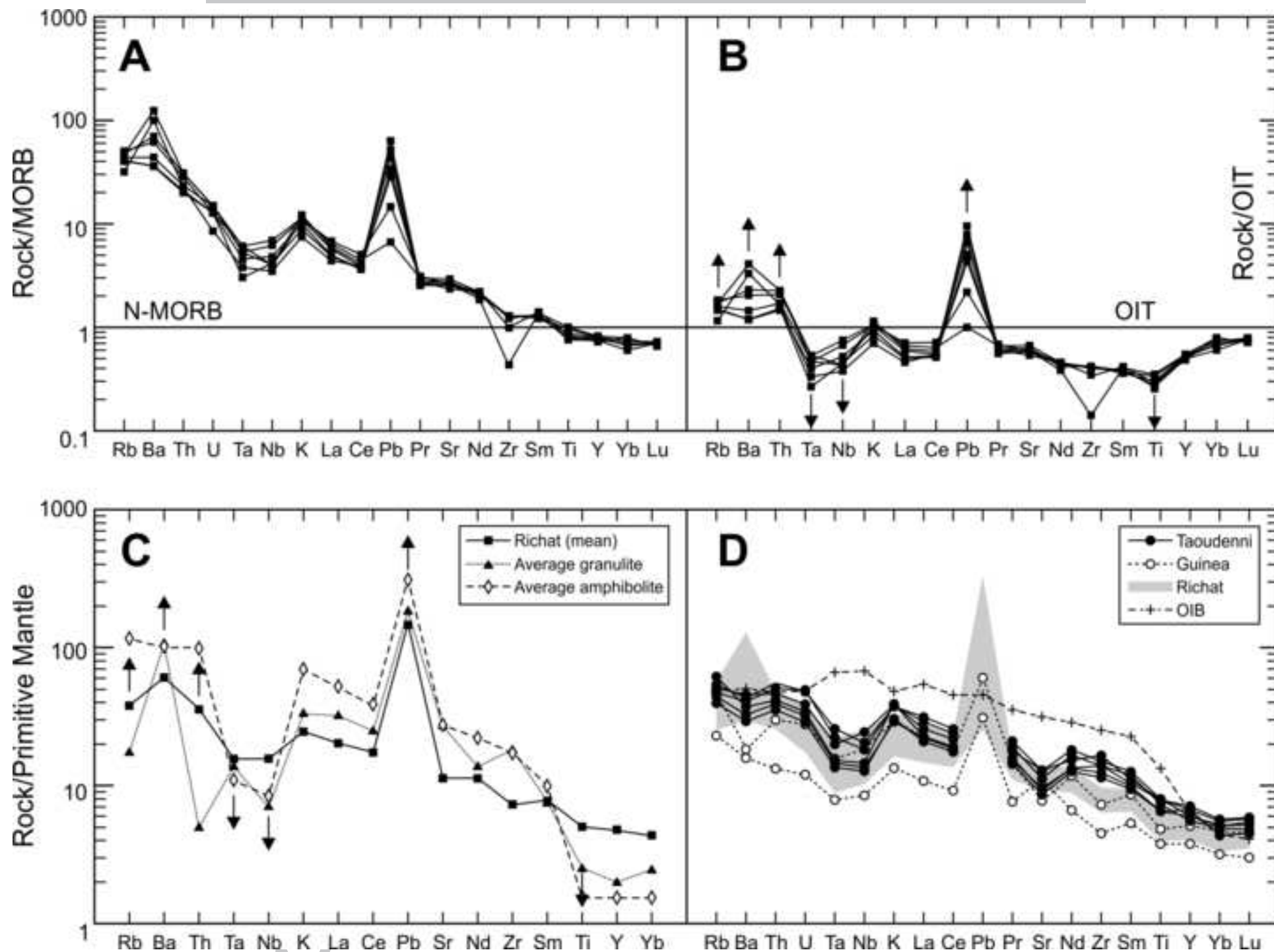


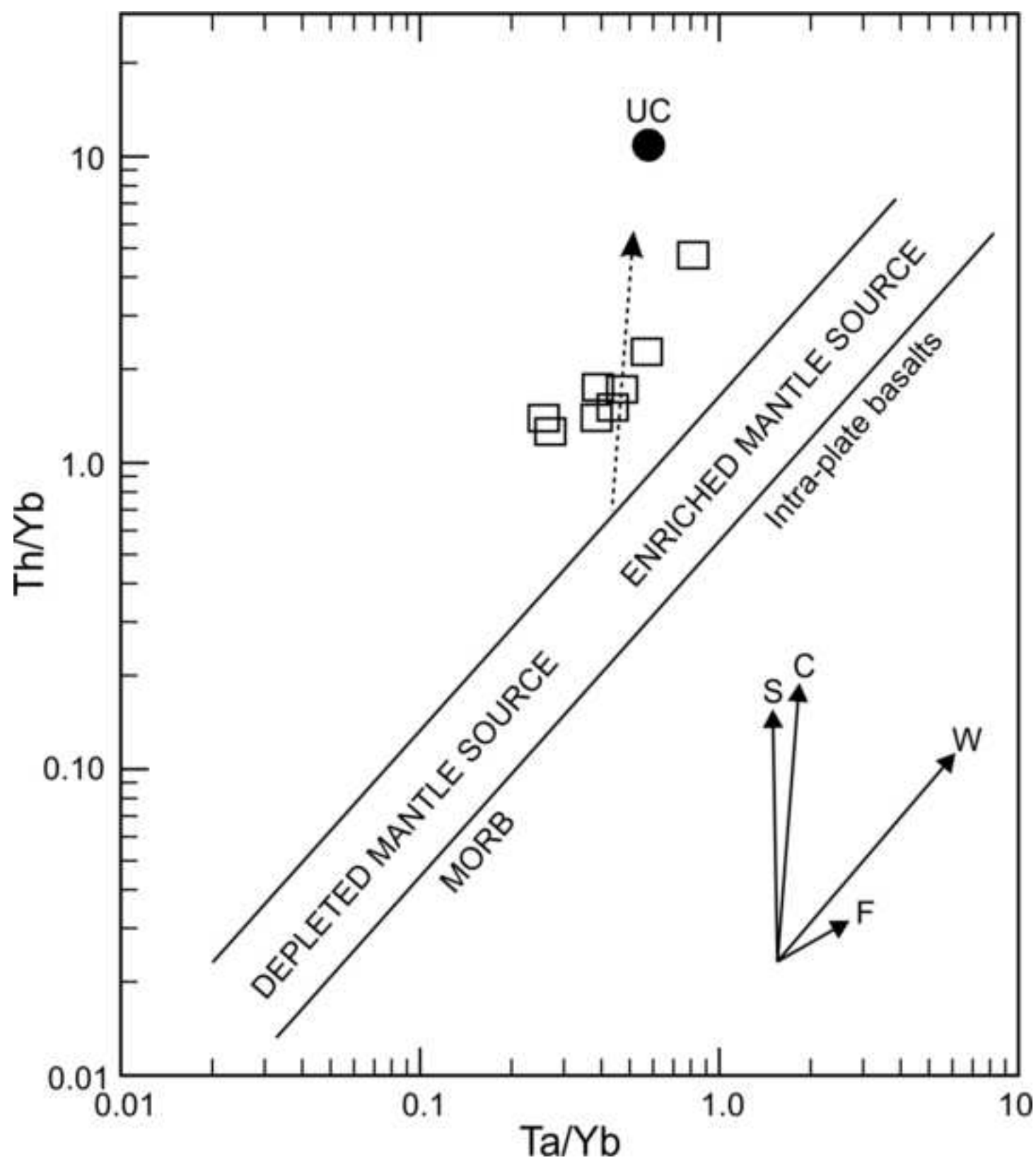


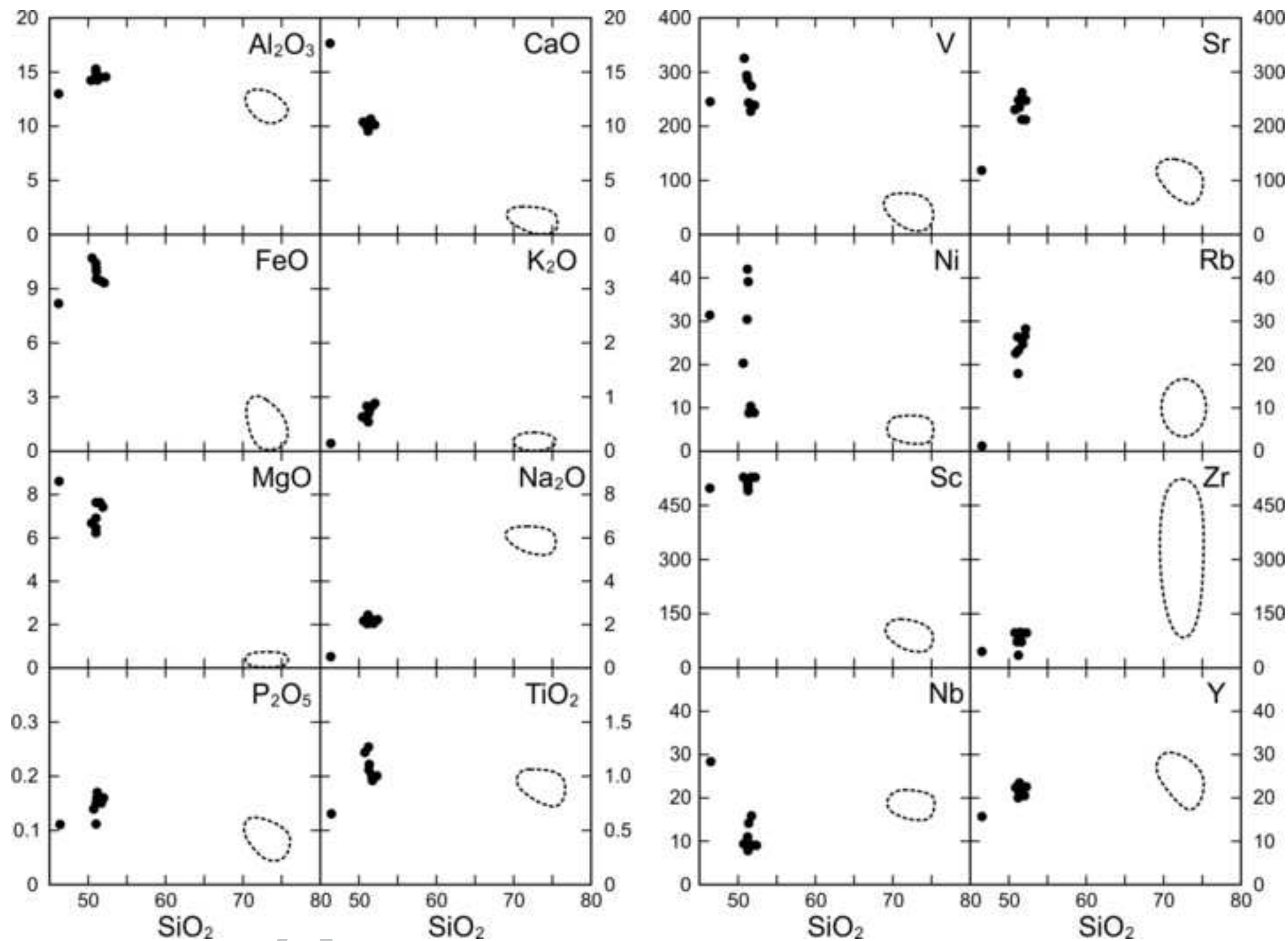


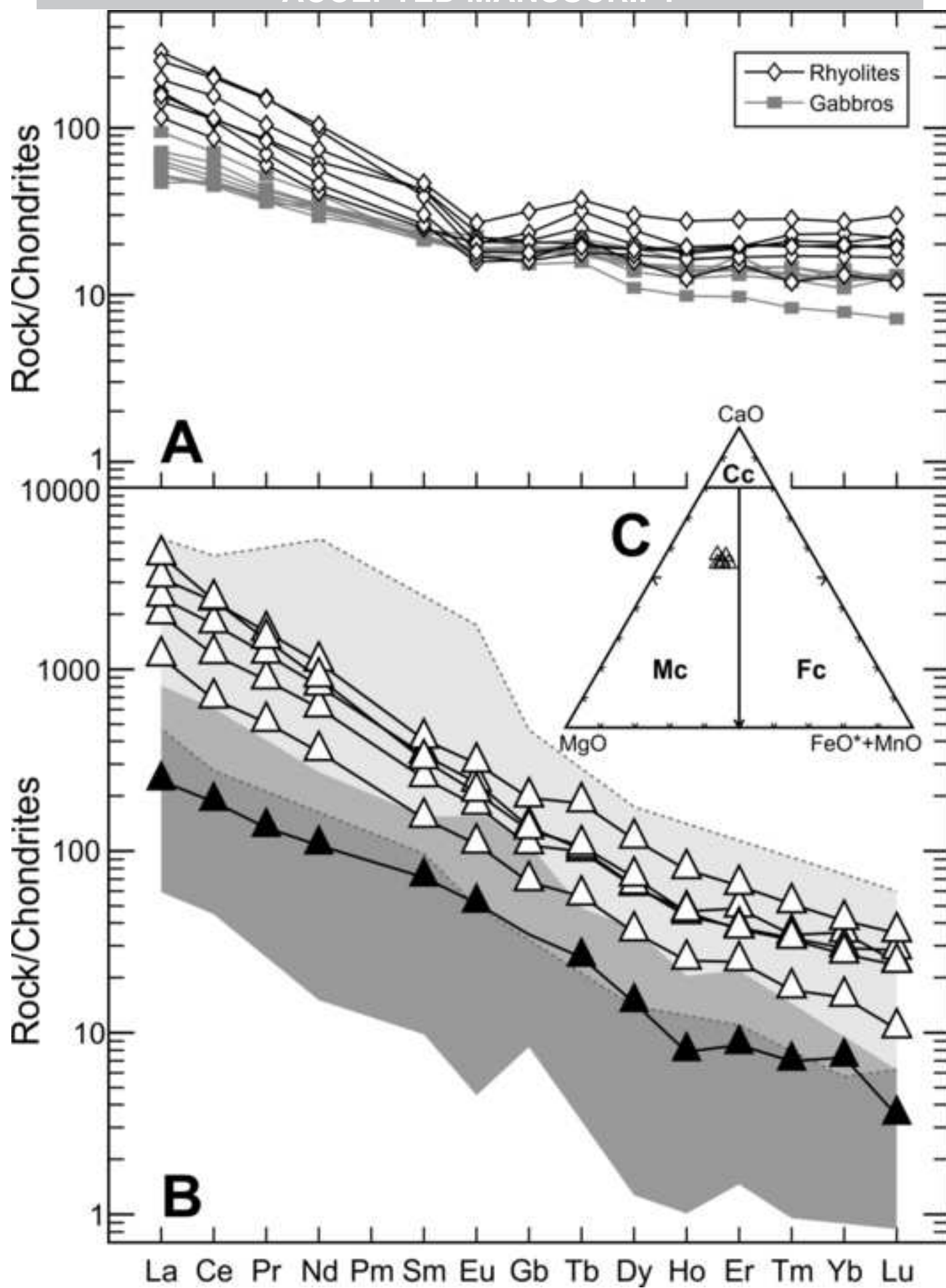
**A****B**

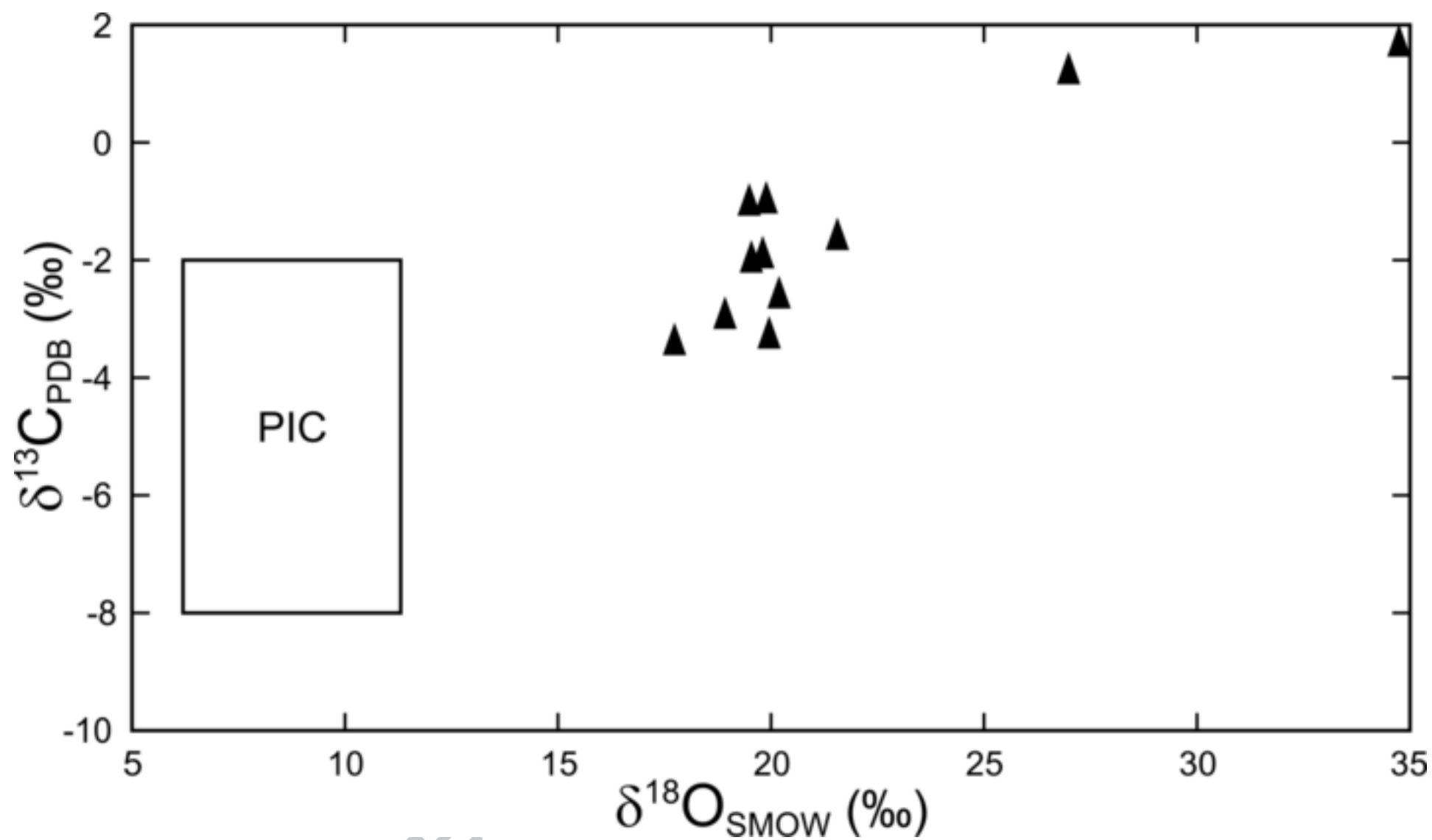












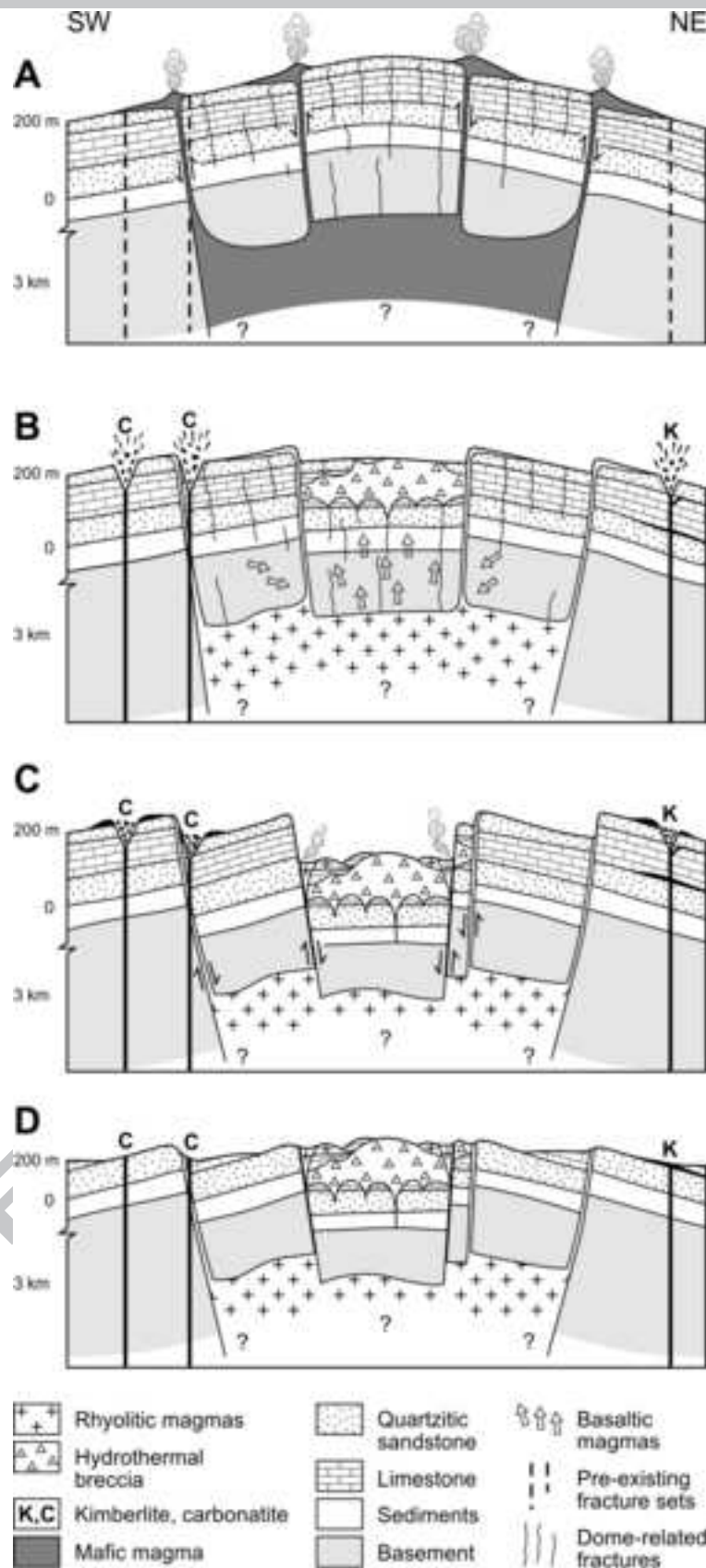
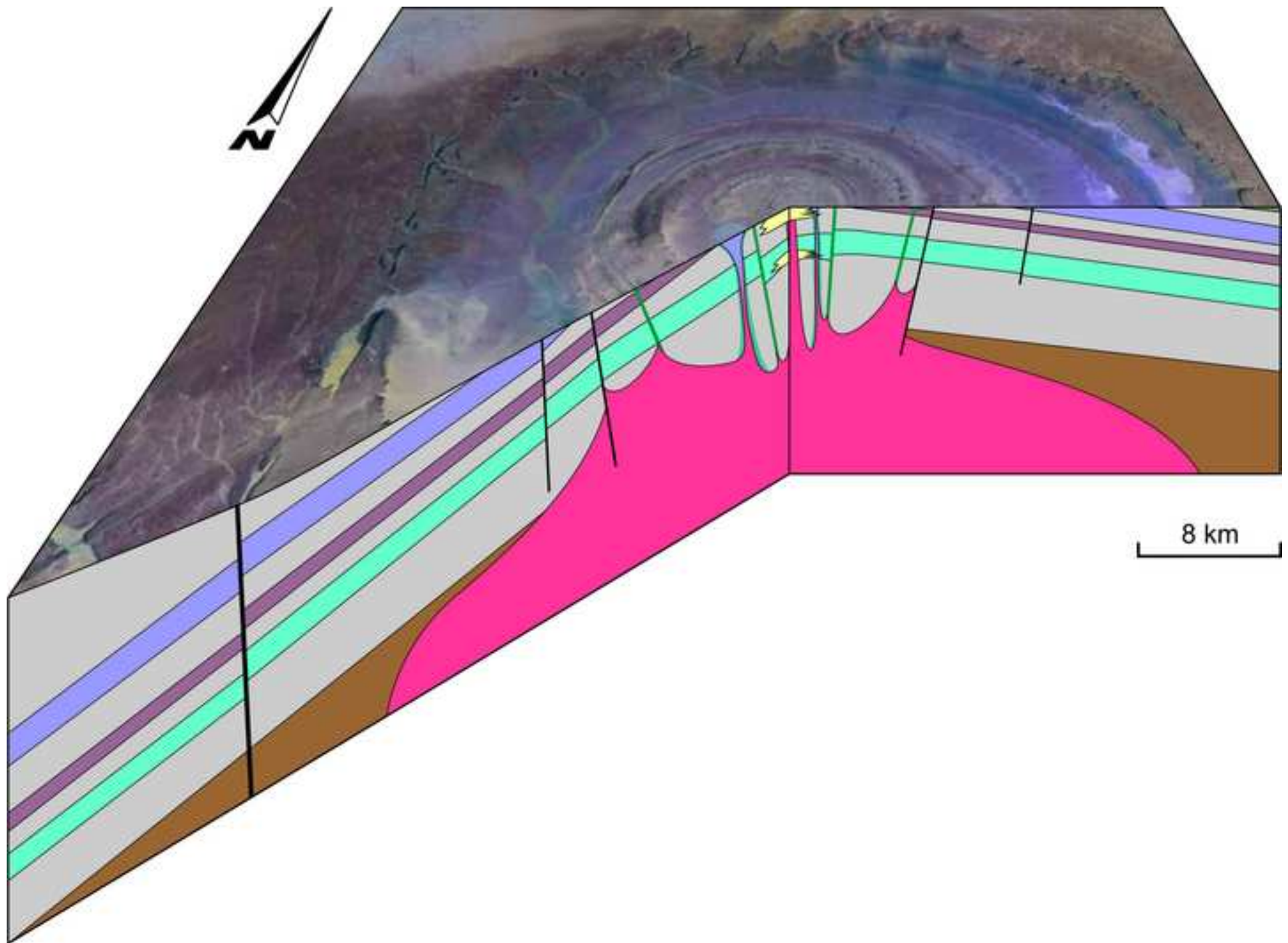


Figure 12



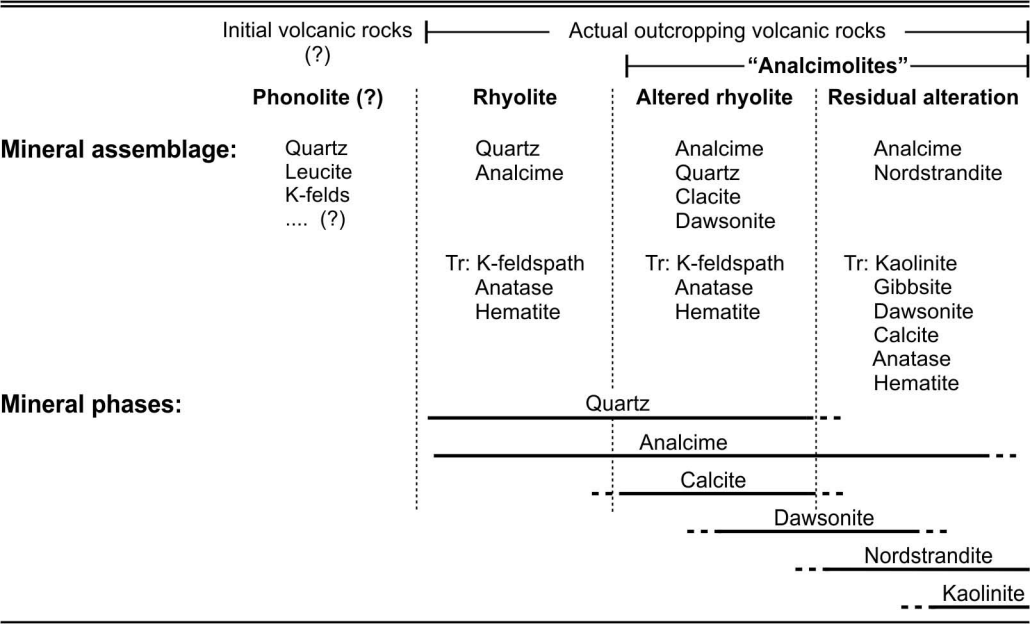
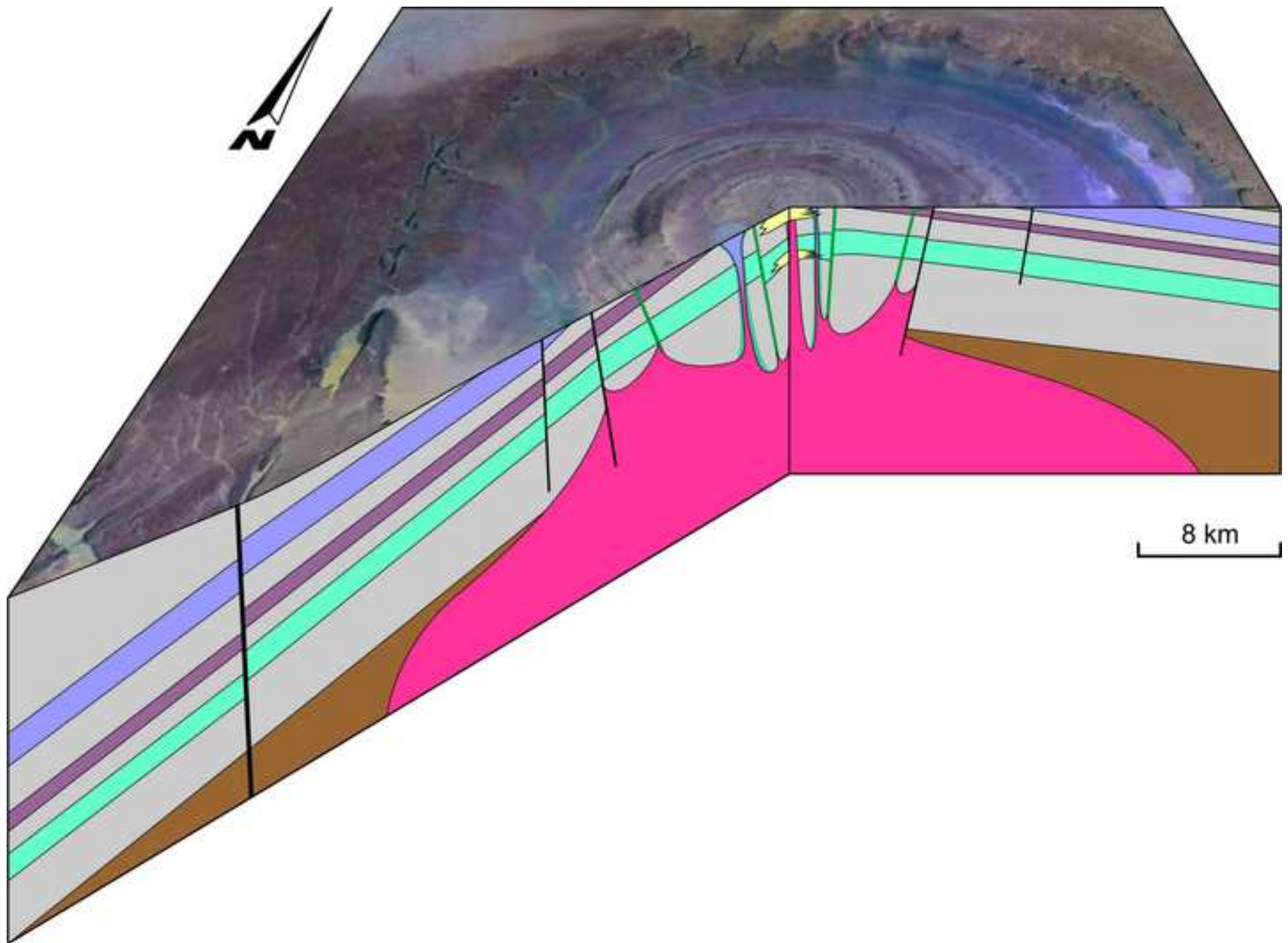


Table	elements	unit	analcime-bearing volcanic rocks	analcime-bearing volcanic rocks	analcime-bearing volcanic rocks	analcime-bearing volcanic rocks	analcime-bearing volcanic rocks	analcime-bearing volcanic rocks	analcime-bearing volcanic rocks	analcime-bearing volcanic rocks	analcime-bearing volcanic rocks	analcime-bearing volcanic rocks	analcime-bearing volcanic rocks	sandstone	chert	limestone	internal sediment	internal sediment	internal sediment	quartzite
		sample number	48	61	100	103	104	134	145	12	74	75	107	10	38	41	68	67	69	101
	SiO ₂	wt %	55.01	73.41	30.87	42.54	73.71	65.1	39.98	27.99	61.09	45.74	47.05	98.18	89.02	7.37	75.88	80.60	80.21	97.33
	Al ₂ O ₃	wt %	16.95	11.30	8.19	28.33	12.27	15.5	19.05	14.34	15.31	18.03	25.28	0.2	0.2	0.77	10.01	8.35	9.04	0.64
	Fe tot	wt %	0.94	1.03	3.16	2.08	0.78	0.93	19.85	0.79	3.58	17.02	1.82	0.64	1.90	0.73	4.41	1.42	0.54	0.40
	MgO	wt %	0.27	0.17	11.09	0.35	0.09	0.14	0.12	8.17	0.26	0.33	0.26	0.01	1.8	2.56	0.03	0.01	< .01	0.07
	MnO	wt %	0.01	0.00	0.06	0.01	0.01	0.01	0.01	0.08	0.01	0.03	0.01	0.00	0.04	0.02	< .01	< .01	<.01	0.01
	K ₂ O	wt %	0.07	0.12	0.39	0.12	0.15	0.2	0.09	0.09	0.16	0.09	0.17	0.02	0.05	0.24	9.03	7.36	8.22	0.04
	CaO	wt %	2.46	1.33	15.63	1.38	0.46	1.47	0.3	13.34	3.18	2.15	1.74	0.15	2.76	48.17	0.27	0.54	0.34	0.37
	Na ₂ O	wt %	9.11	5.74	4.15	8.27	6.07	7.98	6.39	7.87	6.11	9.15	9.02	0.12	0.06	0.13	0.10	0.09	0.09	0.34
	TiO ₂	wt %	1.20	0.93	0.47	1.44	0.87	0.94	1.13	0.43	1.04	0.85	1.29	0.09	0.00	0.04	0.52	0.49	0.53	0.04
	P ₂ O ₅	wt %	0.11	0.D7	0.07	0.12	0.09	0.12	0.25	0.13	0.18	0.31	0.15	0.Q3	0.01	0.06000	0.16	0.39	0.28	0.02
	Cr ₂ O ₃	wt %	0.009	0.004	0.014	0.035	0.011	0.014	0.017	0.021	0.011	0.015	0.019	0.002	0.003	0.000	0.003	0.002	0.002	0.002
	LOI	wt %	13.30	5.50	25.5	15.00	5.3	7.4	10.5	26.5	8.4	6.01	12.9	0.70	4.05	37.91	1.20	1.20	0.70	0.7
	Total	wt %	99.45	99.60	99.59	99.67	99.81	99.80	97.69	99.75	99.33	99.71	99.71	100.14	99.89	98.00	101.61	100.45	99.95	99.96
	V	ppm	40.0	33.0	38.0	172.0	43.0	137.0	362.0	84.0	47.0	224.0	38.0	6.0	5.0	7.0	31.0	28.0	31.0	6.0
	Co	ppm	0.3	1.0	9.7	1.0	1.9	2.8	2.6	3.0	5.1	21.6	2.3	1.5	1.2	1.2	15.6	7.2	2.6	0.8
	Ni	ppm	8.2	6.4	23.5	13.4	10.1	10.9	30.7	5.2	15.3	40.3	16.9	0.0	0.0	0.0	20.6	9.3	2.1	2.4
	As	ppm	6.0	9.8	2.9	3.6	1.2	1.0	8.9	47.1	7.2	55.6	7.2	0.0	9.9	0.8	30.3	18.5	9.8	1.2
	Rb	ppm	1.5	8.9	41.6	8.5	12.6	19.6	14.1	4.9	7.2	4.8	15.5	1.0	1.8	7.6	269.0	246.0	268.6	1.5
	Sr	ppm	175.0	94.0	284.5	301.7	105.6	125.0	105.8	218.7	156.1	98.5	220.0	23.6	35.2	226.1	139.2	96.9	81.2	33.4
	Zr	ppm	154.2	110.5	195.8	334.6	477.7	493.2	457.1	140.9	773.4	464.0	400.5	264.6	6.3	9.8	183.9	205.1	180.2	41.1
	Bi	ppm	0.3	0.2	>2000	1.0	0.3	0.4	259.0	<.1	0.2	0.1	0.1				< .1	0.1	< .1	2.3
	Sb	ppm	1.1	1.1	0.7	0.6	0.3	0.2	0.6	0.5	0.2	1.0	0.1	0.3	0.6	0.1	2.2	1.1	0.3	0.3
	Ga	ppm	25.0	14.1	8.6	37.5	14.3	22.1	29.6	6.9	15.0	18.9	31.1	1.1	2.6	1.7	15.6	12.5	14.9	1.0
	Nb	ppm	22.1	17.4	20.3	40.9	19.6	18.3	27.3	33.8	25.4	24.3	29.5	8.7	0.7	1.2	68.0	38.1	34.4	2.6
	Cd	ppm	0.1	0.0	0.4	<.1	<.1	0.1	<.1	0.1	0.1	0.1	<.1	0.1	0.3	0.0	0.2	< .1	< .1	0.1
	Cs	ppm	29.4	76.1	54.3	73.8	94.7	24.8	26.1	78.2	45.0	97.3	40.7	0.6	0.2	0.6	1.1	1.0	1.1	2.0
	Ba	ppm	105.0	181.0	140.7	277.7	468.8	482.7	72.8	318.4	228.0	404.0	310.4	393.0	494.0	82.0	3526.0	1505.0	1292.0	415.6
	Hf	ppm	3.8	3.2	4.4	8.3	12.2	12.3	12.3	3.6	20.4	11.4	11.1	3.3	0.0	0.0	4.3	4.1	3.9	0.9
	Ta	ppm	1.2	1.0	4.9	2.0	1.3	1.5	5.7	0.7	1.6	1.2	1.9	0.0	0.0	0.0	0.7	0.7	0.7	0.1
	Pb	ppm	25.6	16.9	45.2	5.2	6.9	12.2	11.8	3.1	8.1	8.5	2.5	13.1	12.7	2.9	3.4	4.4	2.5	7.9
	Zn	ppm	21.2	20.6	24.0	13.0	26.0	35.0	34.0	9.0	27.0	68.0	24.0	8.0	25.0	6.0	62.0	16.0	1.0	14.0
	Ag	ppb	<20	<20	<.1	0.1	<.1	0.1	<.1	<.1	<.1	0.1	0.3				< .1	0.1	< .1	<.1
	Mo	ppm	0.5	0.8	1.3	0.2	0.5	0.4	1.4	0.4	0.5	2.9	0.2	8.5	2.9	3.4	2.5	0.6	0.2	0.3
	Cu	ppm	11.4	7.5	16.3	9.0	5.9	7.3	43.2	73.5	169.1	113.8	57.8	9.2	1.7	3.6	18.0	11.1	4.1	6.2
	Sn	ppm	2.7	2.3	2.0	4.0	2.0	3.0	5.0	1.0	3.0	3.0	4.0	<1	<1	<1	2.0	2.0	2.0	<1
	W	ppm	28.2	11.9	7.9	37.1	18.2	36.5	52.0	3.5	31.3	38.2	36.6	4.7	0.3	0.3	19.0	21.0	13.3	1.1
	Au	ppm	<0.1	<0.1	<.5	1.5	<.5	1.0	2.7	6.3	4.9	4.0	2.7	<.5	<.5	<.5	< .5	1.6	< .5	0.6

Th	ppm	47.2	37.9	299.4	29.5	19.2	34.1	25.3	122.3	25.0	49.4	30.6	220.9	2.0	0.2	105.4	100.0	50.3	34.9
Be	ppm	1.0	1.0	3.0	1.0	2.0	1.0	2.0	2.0	1.0	2.0	<1							<1
Y	ppm	11.9	20.5	75.8	29.0	25.4	29.8	28.6	137.5	46.1	31.4	28.0	49.6	4.3	4.3	61.1	80.7	49.7	13.9
Sc	ppm	8.3	4.6	18.0	14.0	6.0	6.0	18.0	24.0	11.0	11.0	12.0	2.0	1.0	1.0	5.0	2.0	2.0	1.0
U	ppm	1.1	1.5	1.1	3.3	1.7	1.8	2.4	6.7	3.2	2.6	2.2	0.5	0.3	0.4	3.5	4.0	3.3	0.3
La	ppm	23.0	39.0	21.0	67.5	37.2	46.2	52.5	19.0	34.0	27.3	59.5	3.0	0.0	5.3	25.4	25.6	21.9	5.9
Ce	ppm	49.5	67.3	45.5	125.9	69.5	94.9	94.6	47.1	68.8	52.8	122.2	9.6	0.9	9.7	56.9	57.0	48.1	21.0
Pr	ppm	5.3	6.6	6.1	14.4	7.9	9.9	10.7	4.7	8.1	5.7	14.1	1.7	0.1	1.2	6.0	6.2	5.2	1.6
Nd	ppm	18.9	21.3	28.1	45.1	26.1	34.6	32.6	21.8	29.1	19.1	48.5	8.8	0.5	4.2	25.4	26.0	20.8	6.5
Sm	ppm	3.0	4.0	11.0	5.9	4.6	6.4	4.4	10.0	6.5	3.8	7.1	8.4	0.4	0.9	8.6	8.9	6.8	1.5
Eu	ppm	0.7	0.9	3.7	1.0	1.0	1.2	0.8	4.8	1.4	1.2	1.3	3.7	0.2	0.2	2.9	3.1	2.1	0.3
Gd	ppm	2.1	3.3	15.0	3.6	3.3	4.2	3.2	20.0	6.4	4.8	4.3	14.2	0.7	0.7	11.4	12.3	8.5	1.8
Tb	ppm	0.4	0.8	2.8	0.7	0.7	0.8	0.8	5.5	1.4	1.2	0.9	2.5	0.2	0.1	2.2	2.6	1.7	0.4
Dy	ppm	2.7	4.0	15.3	4.7	4.4	4.7	4.7	29.4	7.5	6.1	5.1	11.5	0.9	0.7	11.4	14.4	9.2	2.4
Ho	ppm	0.5	0.7	2.7	1.0	0.9	1.1	1.0	5.3	1.6	1.1	1.0	1.8	0.2	0.1	2.2	2.8	1.7	0.5
Er	ppm	1.9	2.5	7.1	3.2	2.8	3.2	3.3	12.4	4.6	3.3	3.1	3.9	0.0	0.3	5.4	6.9	4.4	1.3
Tm	ppm	0.3	0.3	0.9	0.6	0.4	0.5	0.5	1.5	0.7	0.5	0.5	0.5	0.0	0.0	0.7	0.8	0.6	0.2
Yb	ppm	2.0	2.2	5.5	3.9	2.9	3.4	3.5	7.9	4.6	3.2	3.5	3.1	0.3	0.3	4.2	5.0	3.2	0.8
Lu	ppm	0.2	0.3	0.7	0.6	0.4	0.5	0.5	1.1	0.8	0.5	0.6	0.4	0.0	0.0	0.5	0.7	0.5	0.1



Highlights

- First detailed geological description of the geology of the Richat complex
- Discovery of bimodal tholeitic and alkaline volcanism of cretaceous age
- Superposition of multi-level magmatic chambers in a 100 MA caldera complex